Uranium deposits of Franceville basin (Gabon): Role of organic matter and oil cracking on uranium mineralization

Andreï Lecomte, Raymond Michels, Michel Cathelineau, Christophe Morlot, Marc Brouand, Nicolas Flotte

Uranium deposits of Franceville basin (Gabon): Role of organic matter and oil cracking on uranium mineralization

Andreï Lecomte[1,*], Raymond Michels[1], Michel Cathelineau[1], Christophe Morlot[1], Marc Brouand[2], Nicolas Flotté[2].

[1]GeoRessources, Université de Lorraine, CNRS, CREGU, Boulevard des Aiguillettes B.P. 239 F-54506 Vandœuvre-lès-Nancy, France

[2] ORANO, 125 Avenue de Paris F-92320 Châtillon, France

*Corresponding author: GeoRessources, Boulevard des Aiguillettes B.P. 239 F-54506 Vandoeuvre lès Nancy, France

E-mail address: Andrei.Lecomte@univ-lorraine.fr

Graphical abstract

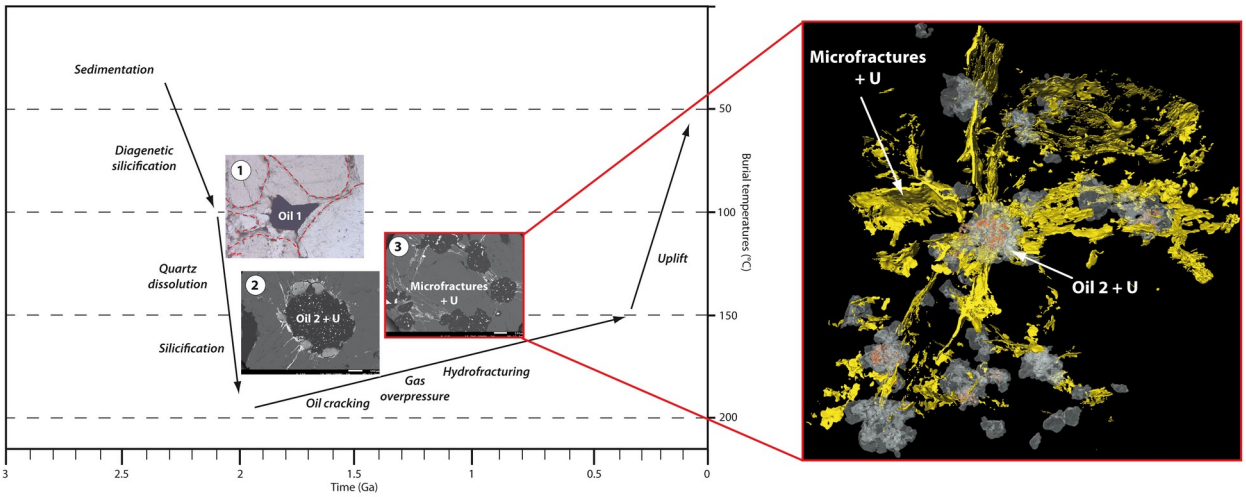

Abstract

The lower Proterozoic uranium deposits in the Franceville basin (Gabon) are mainly known to have hosted natural nuclear reactors. However, this basin also witnessed a former petroleum system which shows major occurrences of uranium ores associated with organic matter. The uranium mineralization is the result of several episodes of oil generation and migration, fluid mixing and hydrofracturing. During burial, at around 2.0 Ga, black shales were heated and expelled hydrocarbons which migrated in underlying sandstones. The first episode of oil migration was synchronous with a silicification event produced by a hot low salinity fluid, as shown by fluid inclusions trapped in quartz overgrowths. The second episode was contemporaneous with quartz dissolution and is characterized by the mixing of hydrocarbons and oxidizing U-bearing brine which resulted in the precipitation of UO_2 inclusions in oil. Then, oil-to-gas conversion generated overpressured gas trapped in pores with uraniferous bitumen nodules. Changes in the stress regime probably favored radial hydrofracturing around bitumen nodules and subsequently the development of a pervasive micro-fracture network. There, UO_2 precipitated together with Cu-Fe sulfides through thermochemical sulfate reduction favored by the presence of hydrocarbons and methane.

Keywords: Uranium; Organic matter; Franceville basin; Hydraulic fracturing; Gas overpressure; X-ray tomography

1. Introduction

In the Paleoproterozoic Franceville Series (Gabon) since the 1960s several high-grade uranium deposits have been discovered around the Oklo-Okélobondo, Bangombé and Mikouloungou areas. Since the discovery of natural nuclear reactions zones at Oklo in 1972, numerous studies have been carried out, in particular considering Oklo deposit as a natural analogue for nuclear waste repository. On the contrary, other deposits were less studied from the point of view of ore genesis. In the Franceville basin, uranium deposits are mainly located at the top of a basal arenaceous formation, below thick black shale series. Previous studies (e.g. Cortial, 1985; Gauthier-Lafaye, 1986; Gauthier-Lafaye & Weber, 1989; Cortial et al., 1990; Mathieu, 1999; Mossmann, 2001; Mossmann *et al.*, 2005) suggested a close link between uranium deposit occurrences and organic matter accumulation, thermal maturation and oil generation/migration. The purpose of this paper is to focus on genetic relationships between organic matter maturation, oil migration, uranium and sulfides precipitation without nuclear reaction overprints. To this end, we studied samples from Okélobondo, Bangombé and Mikouloungou areas, far enough from reactors to preclude any disturbance on petrographic and geochemical features. We propose an updated paragenetic sequence of hydrocarbon emplacement and mineralization and in particular a new insight into hydrofracturing in mineralized sandstones.

2. Geological setting

The Francevillian basin is one of the seven Precambrian basins of the Congo craton. Francevillian sediments are generally discordant on the archean crystalline basement and cover around 35 000 km^2 over most central and eastern Gabon. The Francevillian basin is made up of several intracratonic elementary basins, namely Okondja basin, Booué basin, Lastourville basin and Franceville basin (Fig. 1), the latter hosting all Gabonese uranium deposits (Fig. 2). A comprehensive review of the opening of Francevillian intracratonic basins can be found in Weber *et al.* (2016). Weber (1968) divided sedimentary series into five formations named FA to FE from bottom to top (Fig. 3). FA formation (ca. 100 to 1000 meters from the edges to the center of the basin) is composed of fluviatile coarse sandstones and conglomerates overlain by tidal sandstones. This transition from fluviodeltaic to marine sedimentation is observed throughout the basin. Heavy minerals (zircons, monazite and thorite) are concentrated in coarse sandstones and conglomerates in the lower part of the formation. 400-1000 meters thick FB formation is mainly composed of black shales (ampelites), whose deposition may be related to the worldwide massive black shales event around 2 Ga. Ampelites are interstratified with sandstones (in particular bitumen-rich black sandstones) and dolomites. Near the top of the FB formation, Mn-carbonates become dominant over Fe-carbonates and constitute the protore of the manganese deposits. The transition from Fe-carbonates to Mn-carbonates is a first redox change to a more oxidizing system (Gauthier-Lafaye and Weber, 2003) and

witness of the oxygen enrichment of the atmosphere (Holland, 2002; El Albani et al., 2010, 2014). FC formation (ca. 10-40 meters) is mainly made up with thick-banded cherts and jaspers, associated with dolomite and black shale beds. Overlying FD and FE formations are dominated by volcano-sedimentary series. FD formation is composed of black shales and welded tuffs at the top of the formation. FE formation consists of pyroclastic sandstones interlayered with shales.

The Franceville basin encloses five uranium deposits, from North to South: Boyindzi, Mounana, Oklo-Okélobondo, Bangombé and Mikouloungou. Uranium deposits are located at the top of the FA formation in the vicinity of FA-FB limit. Mineralized areas are therefore related to stratigraphic or tectonic contact between FA sandstones and FB black shales.

In the Franceville basin, organic matter is located in the petroleum source-rocks of the FB formation (ampelites), along migration pathways and in reservoir facies such as FA sandstones or dolomites (e.g. Cortial, 1985; Cortial *et al.*, 1990; Gauthier-Lafaye and Weber, 1989; Mossman *et al.*, 2005). FB ampelites contain high levels of organic matter with Total Organic Carbon ranging from a few percents to 15% in the richest layers. Detailed compositions can be found for instance in Cortial (1985), Gauthier-Lafaye (1986), Ossa-Ossa (2010), or Ngombi-Pemba *et al.* (2014). In mineralized facies association between organic matter and uranium has long been described, based on UO_2 inclusions within bitumen nodules (Cortial, 1985; Cortial *et al.*, 1990; Gauthier-Lafaye and Weber,

1989; Parnell, 1996) and in micro-fractures related to hydrofracturing (Gauthier-Lafaye and Weber, 1989). The deposit of U mineralization is produced by interaction between migrated hydrocarbons and U-bearing brines in a continental rifting geological context (e.g. Gauthier-Lafaye and Weber, 1989; Gauthier-Lafaye, 2006; Boiron *et al.*, 2010). During burial, ampelites reached oil window and hydrocarbons were expelled in FA sandstones. Oxidizing brines led to monazite dissolution and leaching as well as liberation of U (Mathieu et al., 2001). Previous studies (Gauthier-Lafaye and Weber, 1989; Gauthier-Lafaye, 2006) suggested a major tectonic event responsible for major fault reactivation, fluid migration and U mineralization. Hydrocarbons were then trapped in structural high levels at the top of FA reservoirs and mixed with U-bearing fluids circulating in FA sandstones. These petroleum traps, located at footwall anticlines, are controlled by longitudinal normal faults and permeability barriers at FA-FB transition (Ndongo et al., 2016). Fluid circulation and mixing was favored by intense hydrofracturing of previously highly silicified sandstones, related to the development of overpressures in undercompacted zones (Gauthier-Lafaye and Weber, 1989).

3. Sampling and analytical procedure

Sampling procedure aimed at selecting representative black shales, sandstones and silts across the FA-FB limit to focus on relationships between organic matter and uranium mineralization. Samples were taken on several drill cores from Mikouloungou, Bangombé and Mingara. Historical samples from

Oklo-Okélobondo and Leyou locations were also studied (samples kept by ORANO, from COGEMA's drilling campaigns in the 1980s and 1990s). Studies were conducted on thin sections and polished sections, the latter consisting of small rock samples included with Araldite in an aluminum ring of 25 mm diameter.

Petrographical studies were done using optical microscope in reflected light and a FEG SEM JEOL 7600F (hot cathode) with an Oxford Instruments SDD-type EDS spectrometer. Electron microprobe (EPMA) analyses were performed using a CAMECA SX100, with an acceleration voltage of 20 kV and beam current of 20 nA.

Multi-element concentrations in organic matter and Rare Earth Elements concentrations in uraninite were measured using a LA-ICP-MS system composed of a GeoLas excimer laser (ArF, 193 nm, Microlas, Göttingen, Germany) associated with an Agilent 7500c quadrupole ICP-MS. Quantification of the results was achieved using two standards CONOSTAN 500 and NIST SRM 610 (Pearce *et al.*, 1997), and subroutine data processing (Leisen, 2011).

3D relationships between organic matter, uraninite inclusions and fractures in two mineralized sandstones (Okélobondo and Bangombé) were investigated by X-ray microfocus computed tomography (XMCT) using a Phoenix-GE Nanotom S 180kV/15W scanner. Data acquisition for Okélobondo sample was performed at an acceleration voltage of 115 kV and a beam current of 125 μA. The distances between the X-ray source from the detector and between the X-ray source and the sample were 30 mm and 500 mm, respectively. The images acquired after a full

360° rotation had a voxel size of 3 μm^3. Data acquisition for Bangombé sample was performed at an acceleration voltage of 100 kV and a beam current of 80 μA. The distances between the X-ray source from the detector and between the X-ray source and the sample were 50 mm and 313 mm, respectively. The images acquired after a full 360° rotation had a voxel size of 8 μm^3. Three-dimensional reconstruction of the sample was performed using VGStudio Max 2.2 software and images were post-processed with FEI Avizo Fire 9.2 software.

4. Results

4.1. Organic petrography

In FA sandstones, organic matter occurs in two different forms (Fig. 4): massive spheroids/nodules and angular fragments of bitumen with (sub-)conchoidal fractures. Although both bitumen types may coexist in rare samples (Fig. 4h), their relationships with the host rock and in particular detrital grains are rather distinct. Indeed, angular shaped bitumens are located within the sandstone primary porosity, trapped in quartz overgrowths or in residual porosity between overgrowths (Fig. 4a and b). In FA sandstones, angular bitumens are synchronous to or later than silicification. On the contrary, in FB sandstones within black shales, bitumens fill out primary porosity as quartz overgrowths are rare. Bitumens are evidences of an early oil migration which limited sandstone silicification. These bitumen fillings do not contain any uraninite inclusions. Conversely, bitumen nodules, whether barren or mineralized, are located in the secondary porosity, in contact with dissolution surfaces (Fig. 4c). Some heavy

minerals such as zircons are found as dissolution remnants within organic matter (Fig. 4d). Dissolution features and bitumen nodules are generally lined up along weakness areas such as interfaces between detrital grains and overgrowths.

4.2. Trace elements distribution in bitumen

Bitumens in FA sandstones, whether mineralized or not, show important heterogeneities of their reflectance (Fig. 4e and f). In particular, many bitumens display a progressive reflectance drop from core to rim. X-ray mapping suggest that lower reflectance halos (Fig. 4f) contain higher concentrations of U, Cu, Fe and S (Fig. 5) which are not expressed as visible mineral phases under SEM. Trace element concentration in nodules and angular bitumens measured by LA-ICP-MS are presented in Table 1. Only S, Ti, V, Mn, Fe, Ni and Cu concentrations were high enough to be measured accurately. U was not present in our organic standard and was thus not determined. Angular bitumens have low metal concentrations: Ti, V, Mn, Fe, Cu range between a few ppm (often below detection limit) and less than 100 ppm (except for Fe which is up to 275 ppm). Bitumen nodules have higher metal concentration than angular bitumens. Ti, V, Mn and Fe range between a few ppm (up to 182 ppm Fe) and several thousands of ppm. Lower reflectance halos contain higher metal concentration than pristine bitumen cores and angular bitumens in particular. Ti, V, Mn, Fe, Cu concentrations range between tens of ppm (mostly over a hundred ppm) and several tens of thousands ppm (Fig. 6). Difference between concentrations in bitumen and halos is particularly high for Fe and Cu (Fig. 6b).

4.3. Petrography of uranium mineralization

In FA sandstones, uranium distribution is generally linked to the presence of bituminous nodules (Fig. 7). In these nodules, uranium occurs as i) nanometer to micrometer scale inclusions of UO_2 homogeneously disseminated in the bitumen matrix (Fig. 7a). UO_2 inclusions display an angular shape, sometimes close to the cubic shape of euhedral uraninite (Fig. 7b); and as ii) veinlets and fillings of large voids (up to a few millimeters; Fig. 7c and d). UO_2 crystals are trapped with quartz within bitumen voids suggesting that uranium precipitation is sub-synchronous with a major stage of silicification and porosity reduction. It is important to notice that some UO_2 veinlets are elongated and bended underlining bitumen deformation (Fig. 7c). As previously described, uraniferous bitumens and angular bitumen sometimes display alteration halos that are enriched in U, together with Cu and Fe (Fig. 7b and g).

In addition to the uranium mineralization associated with bitumen, an important part of UO_2 in mineralized sandstones is located in micro-fractures and secondary porosity devoid of organic matter (Fig. 7e to h and Fig. 8). UO_2 is also observed in secondary porosity and cements clays (Fig. 8c to e). An additional occurrence of uranium mineralization is within mechanical weakness zones, in particular at the boundaries between detrital grains and overgrowths.

Uraninite is observed in fractures in association with sulfides (pyrite, chalcopyrite, sometimes altered to bornite or chalcocite, and rarely cobaltite or nickeliferous cobaltite) and sulfates as barite (Fig. 7 g and h, Fig. 8f and g). Some UO_2 occurs within sulfide growth zones. Fractures filled with calcite crosscut

mineralized fractures. Rare calcite fillings are found in vugs with radial micro-fractures around.

4.4. Uranium ore crystallochemistry

The different types of uranium mineralization (disseminated inclusions in organic matter, voids in organic matter and fracture fillings, labeled as U1, U2 and U3, respectively) were analyzed with EPMA. Results are listed in table 2 in weight percents for major oxides. Atoms per formula units (APFU) of uranium minerals were calculated on the basis of two oxygens and one cation. In figure 9, U+Ca and Ca+P concentrations are plotted against Si+P and U+Si, respectively. U1, U2 and U3 are aligned between uraninite and coffinite end-members, most analyses close to uraninite, indicating a usual but very limited coffinitization of UO_2. Low analytical totals in uranium minerals are probably related to micro-porosity or hydratation associated with coffinitization (Deditius *et al.*, 2008). In U3, Ca+P concentrations are higher than in U1 and U2, and are above the 1:1 substitution line U↔Ca / Si↔P.

LA-ICP-MS REE analyses are reported in Table 3. REE spectra normalized to chondrite (chondrite REE concentrations after Boynton, 1984) are plotted in Fig. 10. U1 and U2 display a rather similar pattern, with a bell shape, centered on light rare earth elements (LREE) and more or less flattened depending on the localities. However, U2 patterns display a negative Eu anomaly which is not observed in U1 uraninites. U3 REE patterns are highly fractionated between LREE and HREE, in favor of LREE. Some samples also display a positive Eu or

Gd anomaly. Besides, REE enrichment (measured by Σ REE parameter in figure 11a) is highly variable from a few hundred ppm to several thousand ppm and depends on the sample origin. On the contrary, fractionation between LREE and HREE, measured by $(\Sigma \text{ LREE}/\Sigma \text{ HREE})_N$ is similar in U1 and U2 but higher in U3. In figure 11b, Eu anomaly Eu/Eu* is plotted against Y/Σ REE. U1 and U2 uraninites have a similar Y/Σ REE ratio but U2 displays a negative Eu anomaly (Eu/Eu* < 1), which is not observed in U1 (Eu/Eu* = 1). In U3, Y/Σ REE ratio is low and most REE patterns display a highly positive Eu anomaly. This kind of spectra, highly fractionated between LREE and HREE, has already been measured in vein-type or roll-front deposits (Kazakhstan, Mercadier *et al.*, 2011) and monazite spectrum as a possible source of rare earth elements.

4.5. Uranium distribution study by X-ray tomography

Spatial relationships between U1, U2 and U3 were obtained by X-ray computed tomography. Two samples from Okélobondo and Bangombé were scanned to build the 3D representation of bitumen nodule shapes and uraninite distribution.

In Okélobondo sample (Fig. 12a to d), UO_2 occurs as uraninite inclusions in nodules as well as in the surrounding fracture network connecting bitumen nodules. Moreover, fracture density seems to increase with nodule size. The total volume of connected network was calculated and corresponds to 1.7% of the sample. This estimation may be slightly underestimated considering that some isolated objects were ignored because of small size or insufficient contrast, but the

latter have no significant impact on the total volume. Uraninite inclusions in organic matter represent 0.27% (i.e. 0.98 wt% U) of the total sample volume, whereas mineralized fractures represent 0.31% (i.e. 1.13 wt% U).

In Bangombé sample (Fig. 12 e and f), bitumen nodules only contain minor primary UO_2 inclusions but are rimmed by uraniferous halos. UO_2 is also found in a dense fracture network. Grain boundaries are often too thin to be properly selected from the X-ray tomography image background and included in the connected volume, which could have been therefore slightly underestimated. Results show that the volume of uraniferous halos is variable but represents up to 90% of a nodule. The total volume of connected network was calculated and corresponds to 1.5% of the sample volume, close to the results obtained for Okélobondo sample. UO_2 within bitumen represents only 0.005% of the sample volume, i.e. 0.02 wt% U. U mineralization associated with fractures represents 0.70 % of the sample volume, i.e. 2.54 wt% U.

4.6. Micro-fractures as revealed by uranium distribution

The petrographical as well as X-ray tomography study of uranium minerals revealed a singular spatial distribution of micro-fractures (Fig. 4, 7 and 8). Their study in 3D allowed to clearly image their occurrence in space. The images indicate that around bitumen nodules contained in paleopores, fractures develop radially (Fig. 7b, e, f, Fig. 12e and f). When fracture propagation occurred to a sufficient close distance, micro-fractures form a connected network (Fig. 7f, Fig. 12e and f). Several features of fracture initiation and development are

distinguished: (a) a development of fracture network proportional to proximity and size of bitumen nodules. When nodules are too small or too distant, fractures do not create a connected network. When nodules do not have critical size, the connected network does not reach pluricentimeter scale. (b) a preferential direction of major fracture networks, which may be related to the local stress field (Fig. 8a). (c) a development of major networks proportional to silicification. In particular, network connection is favored in completely silicified sandstones (Fig. 8a and b). (d) In partly silicified sandstones, where residual porosity is filled with clays (mostly Fe-chlorites with minor kaolinite and illite), fracturing allows connection with open pores and UO_2 crystallization (Fig. 8c to e).

4.7. Chlorite geothermometry

Chlorites are frequently observed associated with illite in FA sandstones and were reported by several authors (e.g. Gauthier-Lafaye, 1986; Gauthier-Lafaye and Weber, 1989; Mathieu, 1999; Ossa-Ossa, 2010; Bankolé *et al.*, 2015; Ossa-Ossa *et al.*, 2014). They are found in the porosity between corroded detrital grains or in fracture fillings and sometime host part of the mineralization (uranium in fractures, sulfides and sulfates). Interestingly, chlorite compositions can be used as a geothermometer (Cathelineau & Nieva, 1985; Cathelineau, 1988; Vidal *et al.*, 2005; Inoue *et al.*, 2009; Bourdelle *et al.*, 2013). Electron microprobe analyses were carried out on samples from Okélobondo, Bangombé and Mikouloungou. In a Fe/(Fe+Mg) vs Si diagram, all analyses are mainly in the “daphnite” field (or around the daphnite-chamosite boundary) (Fig. 13). This dataset was used to

calculate temperature using geothermometry procedure of Bourdelle *et al.* (2013) and the Si vs R^{2+} diagram (Bourdelle and Cathelineau, 2015; Fig. 14). For Mikouloungou and Bangombé samples, mean calculated temperatures are 195±41°C and 205±21°C, respectively (Table 4). For Okélobondo samples, mean temperatures are much higher (289±46°C), which may be related to the heat influence of nearby natural nuclear reactors.

5. Discussion

5.1. Hydrocarbon emplacement stages HC1 and HC2

As previously described, bitumen is present as massive spheroids/nodules and angular bitumen. In FA sandstones, angular bitumen is synchronous to or later than main silicification stage. Within the FB ampelites formation, unconsolidated sand layers contain bitumen which seems to have prevented silicification. Such features may suggest an early hydrocarbon migration episode called HC1 along unsilicified sandstone drains within FB formation to partially silicified primary porosity in sandstones from FA formation (Fig. 4a and b, Fig. 15).

Bitumen nodules, on the contrary, whether barren or mineralized, are found in contact with dissolution surfaces (along grain contact for instance) and filling secondary porosity (Fig. 4c, Fig. 7b, e and f, Fig. 15). Therefore, quartz dissolution pre-dates or is contemporaneous with bitumen nodule emplacement (called HC2, Fig. 15).

5.2. Uranium emplacement U1 and U2

Accordingly to petrographic observations, oil migration occurred at least twice (HC1 and HC2, Fig. 15) from a common source rock (i.e. FB ampelites) through FA sandstones. Yet, HC1 does not contain uranium inclusions. On the contrary, bitumen nodules (HC2) contain disseminated (sub-)euhedral UO_2 crystals. This observation suggests that a first episode of uranium precipitation (U1) is linked to a mixing of petroleum (HC2) with uranium-bearing fluids leading to reduction of uranyl ions to uraninite, as already suggested by Cortial *et al.* (1990) or Parnell (1996). This model is also supported by fluid inclusion analysis (Mathieu *et al.*, 2000; Dutkiewicz *et al.*, 2007) indicating mixing between brines and liquid hydrocarbons.

Uranium is also present as UO_2 veinlets within bitumen nodules (HC2) which are sometimes elongated and bended following bitumen shape and deformation. These veins inside the nodules probably appear in bitumen that was still ductile and are probably due to deformation and retraction effects during solidification of the bitumen. Thus, we may observe UO_2 crystallization during evolution of oil to bitumen, from small UO_2 disseminated inclusions during oil-water mixing to veinlets when nodules become more and more viscous. While some authors suggested that bitumen evolution was related to radiation-induced polymerization (Eakin and Gize, 1992; Parnell, 1996), we may also consider thermally driven transition from oil to bitumen, which triggers volume decrease by bitumen shrinkage and vug formation (Rasmussen and Krapez, 2000).

Vugs within bitumen are then filled with uranium (U2) and cemented by

quartz. U1 and U2 display highly similar chemical composition and REE patterns, close to uraninites from unconformity-related uranium deposits (Mercadier *et al.*, 2011; Alexandre *et al.*, 2015), although the latter display REE patterns centered on Tb rather than lighter REE such as Pr to Sm. In unconformity-related deposits, UO_2 crystallization is related to the circulation of 120-230°C basinal brines for the leaching of U-bearing minerals (possibly monazites) and subsequent U transportation (Mercadier *et al.*, 2011) and the presence of several potential reducing agents for U precipitation. In the Franceville basin, oxidizing brines led to monazite dissolution and leaching of LREE, U and P. Transport of U and REE in brines was probably favored by chloride complexes (Mathieu et al., 2001). The large drop in LREE content may be explained by the cogenetic crystallization of LREE-rich aluminum phosphate-sulfate minerals (APS), preventing LREE integration in UO_2 structure and leading to a bell-shaped pattern (Gaboreau *et al.*, 2007). In FA sandstones, APS are described in the secondary porosity, associated with chlorite and illite (Ossa-Ossa, 2010; Ossa-Ossa *et al.*, 2014). Besides, REE patterns in U1 and U2 are also similar to those found in uraninites from breccia pipe deposits (Lach, 2012), where U and Cu are transported by oxidized brines at temperatures ranging from 80 to 173°C (Wenrich, 1985). The strong Eu anomaly in U2 could be explained by a change in the redox conditions during the U crystallization succession from U1 to U2.

Chlorite and illite are also found in secondary porosity between corroded quartz grains and overgrowths. Temperatures recorded by chlorites suggest crystallization between 154 and 257°C (mean 203±26°C). These temperatures are

slightly lower than those calculated by Ossa-Ossa *et al.* (2014) with the procedure from Vidal *et al.* (2005), a geothermometer not fully adapted to low P-T conditions, but consistent with previous temperature estimates of 130-200°C for the mineralization based on fluid inclusions (Gauthier-Lafaye & Weber, 1989; Mathieu *et al.*, 2000; Dutkiewicz *et al.*, 2007). Since chlorites crystallize after U2 deposition, the values measured would then set the maximum temperatures for mineralization episodes U1 and U2.

5.3. Uranium emplacement U3

A third stage of uranium deposition (U3) is characterized by UO_2 filling micro-fractures (Fig. 5, Fig. 7e to h, Fig. 8 a, e, f, Fig. 12). These fractures develop radially around bitumen nodules and often form a connected network. U3 mineralization displays different REE patterns, rather close to those measured in monazite, but with a larger fractionation between LREE and HREE (Fig. 10). Highly-fractionated REE patterns were reported in various geological settings such as vein-type or roll-front deposits (Mercadier *et al.*, 2011; Alexandre *et al.*, 2015), which makes it difficult to conclude on their significance.

UO_2 in fractures (U3) is commonly associated with iron/copper sulfides (pyrite, chalcopyrite, bornite, covellite) and barite. This observation suggests the role of sulfur fugacity fS_2 and related processes, H_2S inputs or thermochemical sulfate reduction (TSR), in the formation of copper and iron sulfides contemporaneous with uranium mineralization. Chalcopyrite is earlier than pyrite, with barite representing the last crystallized phase in fractures. Uranium bearing bitumen

nodules (HC2) and less commonly angular bitumen (HC1) present lower reflectance halos at their rims (Fig. 5a, Fig. 7b) which contain systematically the same metals also precipitated as sulfides (Fig.7 g and h). It appears that elements involved in fracture fillings (U, Fe, Cu, S) correspond to those found in bitumen reflectance halos. Reflectance variations and halos in kerogen and bitumen at the micrometer scale is often the indication of radiolytic damage in the Franceville basin (Mossman and Nagy, 1996). Together with the increased concentrations in V, Ni, Fe and Cu, this suggests interactions with mineralizing fluids.

We thus propose that uranium occurring in micro-fractures and bitumen rims alteration (halos) is contemporaneous with sulfate reduction leading to copper sulfides and chalcopyrite precipitation, followed by pyrite and then barite.

5.4. Mineralization emplacement and scenario

The paragenetic sequence indicates that the primary U ore formation corresponds to the burial history of the sediments coinciding with the P-T pair favoring oil formation.

During burial diagenesis, the pressure-solution process lead to silica redistribution and local FA sandstones silicification. In the meantime, the progressive thermal maturation of organic matter in black shales results in the production of hydrocarbons, and their subsequent expulsion. The latter are then trapped in nearby reservoirs, such as the FA sandstones, in particular in residual porosity between overgrowth boundaries (leading to the “angular bitumen” as called in the petrographic section) as well as within quartz overgrowths. This stage

is sub-synchronous with the circulation of a hot low salinity fluid trapped in quartz overgrowths and previously described as “Type 1” (4 wt% NaCl, 180°C) in Gauthier-Lafaye & Weber, 1989 and Lw (2.2-8.5 wt% NaCl, 200±10°C) in Mathieu *et al.*, 2000. This fluid is considered as a meteoric recharge that was heated up through its migration in the basement and flowed upward in FA sandstones along major N-S faults (Mathieu *et al.*, 2000).

The second phase (Fig. 15) is marked by quartz dissolution. Important secondary porosity is created by dissolution of the previous overgrowths and detrital grains (Fig. 4c). This porosity is filled by clays (chlorite and illite), calcite and accompanied by a second stage of oil trapping leading to the bitumen nodules. Most bitumen nodules host disseminated uraniferous inclusions and UO_2 veinlets form creep patterns (U1). The most massive nodules have cracks or voids (probably resulting from the retraction of bitumen as it polymerized) filled with UO_2 patches (U2) cemented by SiO_2. Bituminous nodules in FA sandstones are thus related to a second stage of oil trapping, synchronous or later than massive quartz dissolution and acted as a reducing agent for U. The U ores result probably from the interaction between bitumen and basinal brines, a process eventually strengthened by the dilution of the brines by meteoric fluids (Mathieu *et al.*, 2000). According to Mathieu (1999), these fluids, dominated by Na-Ca-Cl and rich in Li, SO_4 and Br, are in equilibrium with sulfates (anhydrite, gypsum and accessory barite) which had been reported by Gauthier-Lafaye and Weber (1989, 2003) as cements in sandstones within upper FA formation. The discordant limit of sulfate-cemented sandstones over the bedding indicates dissolution-

precipitation processes during diagenesis. These brines circulated through basal FA conglomerates and are responsible for REE, P and U leaching (Mathieu et al., 2001). This is in accordance with the findings of Gauthier-Lafaye (1986), Gauthier-Lafaye and Weber (1989, 2003), Mathieu et al. (2000), Gauthier-Lafaye (2006), Bankole et al. (2016) who suggest that oxygenated ground waters leached the FA formation long after deposition of the sediments.

A third stage of uranium deposition (U3) is related to the formation of micro-fracture networks with radial distribution around bitumen. Filled pores and their interconnection accordingly to pore size and inter-distances as to create a complex network is typical of the space distribution of U3 mineralization. Such microfracturing can be related to the stages of hydraulic fracturing in the Franceville basin already inferred by Gauthier-Lafaye and Weber (1989).

Such textures display similarities with those described by Marquez and Mountjoy (1996) in reservoir rocks from the Alberta basin, where subhorizontal and radial fractures extend from vugs and intercrystalline pores. While tectonic stresses may not be completely ruled out, in particular for the development of main oriented fractures, failure initiation occurs as radial micro-fractures around pores filled with hydrocarbons. The strict spatial relationships between bitumen-filled pores and microfracture development suggests that thermal cracking of oil produced gas overpressure and triggered fracturing.

Barker (1990) demonstrated that thermal cracking of oil generates great amounts of gas and a volume increase of up to 400 times. If an isolated reservoir is completely filled with oil, then cracking of as little as 1% of the crude oil is

enough to obtain pressures higher than lithostatic. His model was however based on the conversion of oil to methane and a carbonaceous residue with a complete conversion at 150°C. Yet, it appears that oil is much more stable than considered by the kinetic model used by Barker (1990), up to temperatures as high as 200°C (e.g. Schenk et al, 1997; Domine *et al.*, 1998; Vandenbroucke e al., 1999; Waples, 2000). Tian *et al.* (2008) rather used a full suite of gaseous components to represent oil to gas conversion, which is dominated by C1-C5 gases (Schenk *et al.*, 1997; Waples, 2000). Results show that oil is stable to about 160°C and complete conversion occurs at 210°C, considering a heating rate of 2°C/m.y. Oil conversion into gas at temperatures between 160°C and 200°C is therefore a major drive for gas formation in the tight silicified FA sandstones reservoir.

Tian *et al.* (2008) calculated volume and pressure changes in an isolated reservoir with 100% and 50% oil saturation. In the first case, overpressure may initiate fracturing above 200°C, corresponding to an oil destruction of 95%. In the second case, considering the lower compressibility of water compared to gases and gas dissolution in water, the maximum temperature before fracturing is 195°C, corresponding to an oil destruction of about 86%.

Numerous studies have been conducted to model fracture propagation in rocks (Ghani *et al.*, 2013 and references therein). In particular, in the case of a homogeneous medium within an isotropic domain, it appears that fracturing occurs radially around overpressure source points. Considering a vertical gravitational load applied on a homogeneous material, fracture geometry is defined by deviatoric stresses: horizontal extension initiates vertical mode I hydrofractures,

whereas compressive state of stress leads to conjugate shear fractures (Ghani *et al.*, 2013).

We thus propose that thermal cracking of oil at temperatures close to that of maximal burial (200°C; Gauthier-Lafaye & Weber, 1989; Mathieu et al, 2000; Dutkiewicz *et al.*, 2007) induced gas overpressures which played a major role in the hydrofracturing process.

There is a direct relationship between the hydraulic fracturing mechanism and the location of uranium ore in the studied deposits. The newly formed permeability network caused by hydraulic fracturing allowed circulation of the uranium-bearing fluid and then ore formation.

Since hydraulic fracturing is related to hydrocarbon gases overpressure, it is also proposed that dissolved hydrocarbons (e.g. methane; Dargent *et al.*, 2015) are the reducing agent for uranium. The precipitation of sulfides may be triggered by reduced sulfur provided by the reaction of hydrocarbons (gases as well as bitumen) with dissolved sulfate through TSR at temperatures above 150°C (Machel, 2001). The formation of dissolved sulfides through TSR reactions may also be considered as a potential reducing agent for uranium. In particular, hydrogen sulfide is a candidate for U(VI) reduction despite slow reaction kinetics at rather low temperature which may require previous adsorption on organic matter or minerals like clays (Granger and Warren, 1969; Spirakis, 1981, 1996).

Therefore, we should consider two main events responsible for uranium mineralization in the Franceville basin: (a) during burial at around 2.0 Ga, oil migrated from black shales to sandstones and mixed with uranium bearing brines

to form UO_2 inclusions within bitumen (U1+U2); (b) during uplift, deviatoric stresses were modified and allowed gas overpressure release by hydrofracturing, starting with radial fractures. These micro-fractures could expand and connect to create a network in which UO_2 (U3) and sulfides could precipitate with the presence of CH_4 and H_2S in conditions compatible with TSR. Major differences between U1+U2 and U3 (i.e. REE patterns, volume differences calculated with tomography) support this consideration and preclude any significant remobilization of primary uranium mineralization during hydrofracturing.

6. Conclusions

Main conclusions are the followings:

- The lower Proterozoic uranium deposits in the Franceville basin (Gabon) display a clear association between uranium ore and bitumens, which represent migrated oil within a petroleum system. Thus, U-ores result from a multi-stage mixing process between uranium-bearing brines and liquid or gaseous hydrocarbons controlled by sandstone porosity and hydrofracturing.
- Uranium was first precipitated (U1) at around 2.0 Ga when U-bearing brine interacted with oil expelled from FB and trapped in the FA sandstone reservoir. While petroleum evolved into bitumen, generation U2 of uranium precipitated. Meanwhile quartz cementation reduced significantly the porosity and hydrocarbon cracking during maximum burial temperature led to gas overpressure. Fluid overpressure together

with changes in the stress field favored hydrofracturing. Dissolved hydrocarbons then acted as reducing agent for sulfur through TSR, leading to Cu-Fe sulfides as well as U precipitation (U3).

This study reveals:

- The important role of petroleum systems in the control of metal precipitation, and the development of peculiar conditions favoring fissure permeability increase, and reduction conditions necessary for sulfide and U oxide precipitation.
- The effect of the organic matter evolution through diagenesis and thermal maturation leading to oil and then gas which participated to chemical and mechanical evolution of the reservoirs.

Acknowledgments

The authors would like to thank all members of AREVA Gabon, for welcoming us in Franceville and for their technical assistance in the sampling process. We thank S. Mathieu and O. Rouer for SEM/EPMA results and C. Peiffert for LA-ICP-MS analyses. We also thank E. Gaucher and an anonymous reviewer for their useful comments and suggestions.

This work was supported by ORANO through CREGU research project.

References

Alexandre, P., Kyser, K., Layton-Matthews, D., Joy, B., Uvarova, Y., 2015. Chemical Compositions of Natural Uraninite. The Canadian Mineralogist 53, 595–622.

Bankole, O.M., El Albani, A., Meunier, A., Gauthier-Lafaye, F., 2015. Textural and paleo-fluid flow control on diagenesis in the Paleoproterozoic Franceville Basin, South Eastern, Gabon. Precambrian Research 268, 115–134.

Bankole, O.M., El Albani, A., Meunier, A., Rouxel, O.J., Gauthier-Lafaye, F., Bekker, A., 2016. Origin of red beds in the Paleoproterozoic Franceville Basin, Gabon, and implications for sandstone-hosted uranium mineralization. American Journal of Science 316, 839–872.

Barker, C., 1990. Calculated volume and pressure changes during the cracking of oil and gas in reservoirs. AAPG Bulletin 74, 1254–1261.

Boiron, M.C., Cathelineau, M., Richard, A., 2010. Fluid flows and metal deposition near basement/cover unconformity: lessons and analogies from Pb–Zn–F–Ba systems for the understanding of Proterozoic U deposits. Geofluids 10, 270–292.

Bourdelle, F., Cathelineau, M., 2015. Low-temperature chlorite geothermometry: a graphical representation based on a T-R2+-Si diagram. European Journal of Mineralogy 27, 617–626.

Bourdelle, F., Parra, T., Chopin, C., Beyssac, O., 2013. A new chlorite

geothermometer for diagenetic to low-grade metamorphic conditions. Contributions to Mineralogy and Petrology 165, 723–735.

Boynton, W.V., 1984. Cosmochemistry of the rare earth elements: meteorite studies, in: Henderson, P. (Ed.), Rare Earth Element Geochemistry. Elsevier Sci. Publ. Co., Amsterdam, pp. 63–114.

Cathelineau, M., 1988. Cation site occupancy in chlorites and illites as a function of temperature. Clay Minerals 23, 471–485.

Cathelineau, M., Nieva, D., 1985. A chlorite solid solution geothermometer the Los Azufres (Mexico) geothermal system. Contributions to Mineralogy and Petrology 91, 235–244.

Cortial, F., 1985. Les bitumes du Francevillien (Protérozoïque inférieur du Gabon, 2000 Ma) et leurs kérogènes. Relations avec les minéralisations uranifères. PhD Thesis, Université Louis Pasteur, Strasbourg, 183 p.

Cortial, F., Gauthier-Lafaye, F., Lacrampe-Couloume, G., Oberlin, A., Weber, F., 1990. Characterization of organic matter associated with uranium deposits in the Francevillian formation of Gabon (lower proterozoic). Organic Geochemistry 15, 73–85.

Dargent, M., Truche, L., Dubessy, J., Bessaque, G., Marmier, H., 2015. Reduction kinetics of aqueous U(VI) in acidic chloride brines to uraninite by methane, hydrogen or C-graphite under hydrothermal conditions: Implications for the genesis of unconformity-related uranium ore deposits. Geochimica et Cosmochimica Acta 167, 11–26.

Deditius, A.P., Utsunomiya, S., Ewing, R.C., 2008. The chemical stability of

coffinite, $USiO_4 \cdot nH_2O$; $0<n<2$, associated with organic matter: A case study from Grants uranium region, New Mexico, USA. Chem. Geol. 251, 33–49.

Dominé, F., Dessort, D., Brévart, O., 1998. Towards a new method of geochemical kinetic modelling:implications for the stability of crude oils. Organic Geochemistry 28, 597–612.

Dutkiewicz, A., George, S.C., Mossman, D.J., Ridley, J., Volk, H., 2007. Oil and its biomarkers associated with the Palaeoproterozoic Oklo natural fission reactors, Gabon. Chemical Geology 244, 130–154.

Eakin, P.A., Gize, A.P., 1992. Reflected-light microscopy of uraniferous bitumens. Mineralogical magazine 56, 85–99.

El Albani, A., Bengtson, S., Canfield, D.E., Bekker, A., Macchiarelli, R., Mazurier, A., Hammarlund, E.U., Boulvais, P., Dupuy, J.-J., Fontaine, C., Fürsich, F.T., Gauthier-Lafaye, F., Janvier, P., Javaux, E., Ossa, F.O., Pierson-Wickmann, A.-C., Riboulleau, A., Sardini, P., Vachard, D., Whitehouse, M., Meunier, A., 2010. Large colonial organisms with coordinated growth in oxygenated environments 2.1 Gyr ago. Nature 466, 100–104.

El Albani, A., Bengtson, S., Canfield, D.E., Riboulleau, A., Rollion Bard, C., Macchiarelli, R., Ngombi Pemba, L., Hammarlund, E., Meunier, A., Moubiya Mouele, I., Benzerara, K., Bernard, S., Boulvais, P., Chaussidon, M., Cesari, C., Fontaine, C., Chi-Fru, E., Garcia Ruiz, J.M., Gauthier-Lafaye, F., Mazurier, A., Pierson-Wickmann, A.C., Rouxel, O.,

Trentesaux, A., Vecoli, M., Versteegh, G.J.M., White, L., Whitehouse, M., Bekker, A., 2014. The 2.1 Ga Old Francevillian Biota: Biogenicity, Taphonomy and Biodiversity. PLOS ONE 9, e99438.

Feybesse, J.L., Johan, V., Triboulet, C., Guerrot, C., Mayaga-Mikolo, F., Bouchot, V., Eko N'dong, J., 1998. The West Central African belt: a model of 2.5–2.0Ga accretion and two-phase orogenic evolution. Precambrian Research 87, 161–216.

Gaboreau, S., Cuney, M., Quirt, D., Beaufort, D., Patrier, P., Mathieu, R., 2007. Significance of aluminum phosphate-sulfate minerals associated with U unconformity-type deposits: The Athabasca basin, Canada. American Mineralogist 92, 267–280.

Gauthier-Lafaye, F., 1986. Les gisements d'uranium du Gabon et les réacteurs d'Oklo. Modèle métallogénique de gîtes à fortes teneurs du Protérozoïque inférieur, Sciences Géologiques, bulletins et mémoires.

Gauthier-Lafaye, F., 2006. Time constraint for the occurrence of uranium deposits and natural nuclear fission reactors in the Paleoproterozoic Franceville Basin (Gabon). Memoir of the Geological Society of America 198, 157–167.

Gauthier-Lafaye, F., Weber, F., 1989. The Francevillian (Lower Proterozoic) uranium ore deposits of Gabon. Economic Geology 84, 2267–2285.

Gauthier-Lafaye, F., Weber, F., 2003. Natural nuclear fission reactors: Time constraints for occurrence, and their relation to uranium and manganese deposits and to the evolution of the atmosphere. Precambrian Research

120, 81–100.

Ghani, I., Koehn, D., Toussaint, R., Passchier, C.W., 2013. Dynamic Development of Hydrofracture. Pure and Applied Geophysics 170, 1685–1703.

Granger, H.C., Warren, C.G., 1969. Unstable sulfur compounds and the origin of roll-type uranium deposits. Economic Geology 64, 160-171.

Holland, H.D., 2002. Volcanic gases, black smokers, and the great oxidation event. Geochimica et Cosmochimica Acta 66, 3811–3826.

Inoue, A., Meunier, A., Patrier-Mas, P., Rigault, C., Beaufort, D., Vieillard, P., 2009. Application for chemical geothermometry to low-temperature trioctahedral chlorites. Clays and Clay Minerals 57, 371–382.

Lach, P., 2012. Signature géochimique des éléments des terres rares dans les oxydes d'uranium et minéraux associés dans les gisements d'uranium : analyse par ablation laser couplée à l' ICP-MS et étude géochronologique. PhD Thesis, Université de Lorraine, 295 p.

Leisen, M., 2011. Analyse chimique des inclusions fluides par ablation-laser couplée à l'ICP-MS et applications géochimiques. PhD Thesis, Nancy-Université, 318 p.

Machel, H.G., 2001. Bacterial and thermochemical sulfate reduction in diagenetic settings – old and new insights. Sedimentary Geology 140, 143–175.

Marquez, X., Mountjoy, E., 1996. Microfractures due to overpressures caused by thermal cracking in well-sealed Upper Devonian Reservoirs, Deep Alberta Basin 80.

Mathieu, R., 1999. Reconstitution des paléocirculations fluides et des migrations élémentaires dans l'environnement des réacteurs nucléaires naturels d'Oklo (Gabon) et des argilites de Tournemire (France). PhD Thesis, Institut National Polytechnique de Lorraine, 350 p.

Mathieu, R., Cuney, M., Cathelineau, M., 2000. Geochemistry of palaeofluids circulation in the Franceville basin and around Oklo natural nuclear reaction zones (Gabon). Journal of Geochemical Exploration 69–70, 245–249.

Mathieu, R., Zetterström, L., Cuney, M., Gauthier-Lafaye, F., Hidaka, H., 2001. Alteration of monazite and zircon and lead migration as geochemical tracers of fluid paleocirculations around the Oklo–Okélobondo and Bangombé natural nuclear reaction zones (Franceville basin, Gabon). Chemical Geology 171, 147–171.

Mercadier, J., Cuney, M., Lach, P., Boiron, M.C., Bonhoure, J., Richard, A., Leisen, M., Kister, P., 2011. Origin of uranium deposits revealed by their rare earth element signature. Terra Nova 23, 264–269.

Mossman, D.J., 2001. Hydrocarbon habitat of the Paleoproterozoic Franceville Series, Republic of Gabon. Energy Sources 23, 45–53.

Mossman, D.J., Gauthier-Lafaye, F., Jackson, S.E., 2005. Black shales, organic matter, ore genesis and hydrocarbon generation in the Paleoproterozoic Franceville Series, Gabon. Precambrian Research 137, 253–272.

Mossman, D.J., Nagy, B., 1996. Solid bitumens: an assessment of their characteristics, genesis, and role in geological processes. Terra Nova 8,

114–128.

Ndongo, A., Guiraud, M., Vennin, E., Mbina, M., Buoncristiani, J.-F., Thomazo, C., Flotté, N., 2016. Control of fluid-pressure on early deformation structures in the Paleoproterozoic extensional Franceville Basin (SE Gabon). Precambrian Research 277, 1–25.

Ngombi-Pemba L., El Albani A., Meunier A., Grauby O., Gauthier-Lafaye F., 2014. From detrital heritage to diagenetic transformations, the message of clay minerals contained within shales of the Palaeoproterozoic Francevillian basin (Gabon). Precambrian Research 255, 63-76.

Ossa Ossa, F., 2010. Etude multi-approches du bassin sédimentaire paléoprotérozoïque (2.1-2.4 Ga) de Franceville au Gabon: les environnements sédimentaires et l'impact des paléocirculations de fluides. PhD Thesis, Université de Poitiers, 191 p.

Ossa Ossa, F., Hofmann, A., Vidal, O., Kramers, J.D., Agangi, A., Belyanin, G.A., Mayaga-Mikolo, F., 2014. Hydrothermal clay mineral formation in the uraniferous Paleoproterozoic FA Formation, Francevillian basin, Gabon. Precambrian Research 246, 134–149.

Parnell, J., 1996. Petrographic relationships between mineral phases and bitumen in the Oklo Proterozoic natural fission reactors, Gabon. Mineralogical Magazine 60, 581–593.

Pearce, N.J.G., Perkins, W.T., Westgate, J.A., Gorton, M.P., Jackson, S.E., Neal, C.R., Chenery, S.P., 1997. A compilation of new and published major and trace element data for NIST SRM 610 and NIST SRM 612 glass

reference materials. Geostandards Newsletter-the Journal of Geostandards and Geoanalysis 21, 115–144.

Préat, A., Bouton, P., Thiéblemont, D., Prian, J.-P., Ndounze, S.S., Delpomdor, F., 2011. Paleoproterozoic high δ13C dolomites from the Lastoursville and Franceville basins (SE Gabon): Stratigraphic and synsedimentary subsidence implications. Precambrian Research 189, 212–228.

Rasmussen, B., Krapez, B., 2000. Evidence of hydrocarbon and metalliferous fluid migration in the Palaeoproterozoic Earaheedy Basin of Western Australia. Journal of the Geological Society 157.

Schenk, H.J., Di Primio, R., Horsfield, B., 1997. The conversion of oil into gas in petroleum reservoirs. Part 1: Comparative kinetic investigation of gas generation from crude oils of lacustrine, marine and fluviodeltaic origin by programmed-temperature closed-system pyrolysis. Organic Geochemistry 26, 467–481.

Spirakis, C.S., 1981. The Possible Role of Sulfate Reduction Kinetics in the Formation of Hydrothermal Uranium Deposit. Economic Geology 76, 2236-2239.

Spirakis, C.S., 1996. The roles of organic matter in the formation of uranium deposits in sedimentary rocks. Ore Geology Reviews 11, 53-69.

Thiéblemont, D., Castaing, C., Billa, M., Bouton, P., Préat, A., 2009. Notice explicative de la Carte géologique et des Ressources minérales de la République gabonaise à 1/1 000 000. Editions DGMG, Ministère des Mines, du Pétrole, des Hydrocarbures. Libreville, 384 p.

Tian, H., Xiao, X., Wilkins, R.W.T., Tang, Y., 2008. New insights into the volume and pressure changes during the thermal cracking of oil to gas in reservoirs: Implications for the in-situ accumulation of gas cracked from oils. AAPG Bulletin 92, 181–200.

Vandenbroucke, M., Behar, F., Rudkiewicz, J.L., 1999. Kinetic modelling of petroleum formation and cracking: implications from the high pressure/high temperature Elgin Field (UK, North Sea). Organic Geochemistry 30, 1105–1125.

Vidal, O., Parra, T., Vieillard, P., 2005. Thermodynamic properties of the Tschermak solid solution in Fe-chlorite: Application to natural examples and possible role of oxidation. American Mineralogist 90, 347–358.

Waples, D.W., 2000. The kinetics of in-reservoir oil destruction and gas formation: constraints from experimental and empirical data, and from thermodynamics. Organic Geochemistry 31, 553–575.

Weber, F., 1968. Une série précambrienne du Gabon: le Francevillien. Sédimentologie, géochimie, relations avec les gîtes minéraux associés., Mém. Serv. Carte Géol. Als. Lorr.

Weber, F., Gauthier-Lafaye, F., Whitechurch, H., Ulrich, M., El Albani, A., 2016. The 2-Ga Eburnean Orogeny in Gabon and the opening of the Francevillian intracratonic basins: A review. Comptes Rendus Geoscience 348, 572–586.

Wenrich, K.J., 1985. Mineralization of breccia pipes in northern Arizona. Economic Geology 80, 1722–1735.

Table captions

Tab. 1 Metal concentration in bitumen (ppm) from LA-ICP-MS analysis. The type of bitumen (angular or nodules) and the presence of low reflectance halos are indicated.

Tab. 2 Composition of uraninite in FA sandstones determined by EPMA in weight percents of major oxides.

Tab. 3 Rare Earth Element concentrations in FA uraninites (ppm) from LA-ICP-MS analysis.

Tab. 4 Composition of Fe-chlorites determined by EPMA.

Figure captions

Fig. 1. General geological map of Gabon with main palaeoproterozoic basins (adapted from Préat *et al.*, 2011).

Fig. 2. Geological map of Franceville basin with main uranium districts (adapted from Ossa Ossa *et al.*, 2014).

Fig. 3. Stratigraphic column of the Francevillian Series in the Franceville basin (adapted from Gauthier-Lafaye and Weber, 2003). FA, FB, FC, FD and FE formations are described in the text.

Fig. 4. Petrographic features of organic matter in FA sandstones (TL: transmitted light; RL: reflected light). **a.** Bitumen cemented sandstone. **b.** Quartz overgrowths (OG) and bitumen (Bit.) filling residual porosity. **c.** Bitumen nodules on the contact between detrital quartz and overgrowths. **d.** Massive bitumen nodule

crosscutting detrital quartz with preserved refractory zircons (Zrn). **e.** Bitumen nodule and partially dissolved quartz overgrowths. **f.** Low reflectance halo on a bitumen nodule. **g.** Low reflectance halo observed with SEM-BSE. **h.** Rare occurrence of coexisting angular bitumen and nodules.

Fig. 5. U, S, Fe and V X-ray maps of bitumen nodules with low reflectance halos.

Fig. 6. V-Ni and Cu-Fe diagrams of angular bitumens and nodules in FA sandstones (LA-ICP-MS analyses).

Fig. 7. Petrographic features of association between organic matter (black), uranium (Urn, white) and sulfides in FA sandstones. **a.** U nano-inclusions in bitumen nodule. **b.** Bitumen nodule with UO_2 inclusions, low reflectance rim and radial U-filled fractures. **c.** Bitumen nodule with elongated UO_2 inclusions and barite (Brt). **d.** Large UO_2 and UO_2 crystals in the center of a bitumen nodule. Residual porosity is filled by quartz (gray). **e.** Bitumen nodules and fractures filled by UO_2 and sulfides (mainly pyrite, Py). **f.** Circular fracture network (UO_2 and pyrite) connecting bitumen nodules **g.** Bitumen nodule with UO_2 inclusions, low reflectance rim and U-filled fractures (sulfides are pyrite and chalcopyrite). **h.** Bitumen with fractures filled by UO_2 and chalcocite (Cc).

Fig. 8. Petrographic features of fractures in FA sandstones. **a.** Fracture network crosscutting detrital quartz (Qtz) and overgrowths (OG). **b.** Fractures and UO_2 precipitation at the boundary between detrital quartz and overgrowths. **c.** UO_2 precipitation on clays and at the boundary between detrital quartz and overgrowths. **d.** Detail of UO_2 and illites. **e.** Fractures filled by UO_2 and pyrite. **f.** Fractures filled by UO_2 and pyrite.

Fig. 9. U+Ca vs Si+P and Ca+P vs U+Si diagrams of uranium mineralization in FA sandstones (APFU Atoms Per Formula Unit). U1, U2 and U3 are represented by triangles, squares and circles, respectively.

Fig. 10. REE patterns in U1, U2 and U3 uraninites from Mikouloungou, Bangombé and Oklo-Okélobondo locations.

Fig. 11. Σ REE vs $(\Sigma \text{ LREE} / \Sigma \text{ HREE})_N$ and Eu/Eu* vs Y/Σ REE diagrams in U1, U2 and U3 uraninites from Mikouloungou, Bangombé and Oklo-Okélobondo locations.

Fig. 12. 3D views from X-ray tomography on samples from Okélobondo (a to d) and Bangombé (e and f). U1-U2 are in orange, U3 in yellow and bitumen nodules are in transparent white. One video of 3D reconstruction can be downloaded from supplementary materials.

Fig. 13. Fe/(Fe+Mg) vs Si and Al(VI) vs Al(IV) diagrams for Fe-chlorites in Oklo-Okélobondo (green triangles), Bangombé (red squares) and Mikouloungou (blue dots) samples.

Fig. 14. Si vs R^{2+} diagram (Bourdelle & Cathelineau, 2015) for Fe-chlorites in Oklo-Okélobondo (green triangles), Bangombé (red squares) and Mikouloungou (blue dots) samples.

Fig. 15. Summary diagram of oil migration and uranium mineralization in FA sandstones. Additional age data are summarized in Gauthier-Lafaye (2006). Orogeny ages are from Feybesse *et al.*, 1998 and Thiéblemont *et al.*, 2009.A complete list of previous data can be found in Mathieu (1999).

Tab. 1 Metal concentration in bitumen (ppm) from LA-ICP-MS analysis. The type of bitumen (angular or nodules) and the presence of low reflectance halos are indicated.

Location	*Type*	*Point*	*S ppm*	*Ti ppm*	*V ppm*	*Mn ppm*	*Fe ppm*	*Ni ppm*	*Cu ppm*
Bangombé	Nodule (core)	1	19546	8167	378	978	8721	42	73
Bangombé	Nodule (core)	2	5725	2630	252	987	8688	24	196
Bangombé	Nodule (core)	3	3234	1255	41	207	1288	n.d.	21
Bangombé	Nodule (core)	4	2443	571	26	119	2603	n.d.	120
Bangombé	Nodule (halo)	5	56701	1927	2005	1126	74915	392	91610
Bangombé	Nodule (halo)	6	11617	41	1164	138	9432	74	19192
Lastourville	Angular bitumen (core)	7	13466	65	81	10	271	755	6
Lastourville	Angular bitumen (core)	8	9078	4	65	2	206	1254	3
Lastourville	Angular bitumen (core)	9	7749	6	35	n.d.	34	589	1
Lastourville	Angular bitumen (core)	10	5801	2	30	n.d.	22	497	1
Leyou	Nodule (core)	11	5666	422	147	83	670	10	3
Leyou	Nodule (core)	12	5445	42	1728	293	33979	13	16
Leyou	Nodule (core)	13	8829	20	3662	104	1367	22	n.d.
Leyou	Nodule (core)	14	10335	79	6343	203	1267	26	1
Leyou	Nodule (core)	15	5671	404	125	141	496	3	3
Leyou	Nodule (core)	16	6409	484	446	144	6561	6	3
Leyou	Nodule (core)	17	7407	269	5812	941	1173	n.d.	14
Leyou	Nodule (halo)	18	7141	35	15735	2029	1963	62	161
Leyou	Nodule (halo)	19	4647	12	6461	593	1581	34	146
Leyou	Nodule (halo)	20	6350	14	24313	582	6034	32	220
Leyou	Angular bitumen (core)	21	1719	1	n.d.	n.d.	77	12	0,8
Leyou	Angular bitumen (core)	22	2726	10	n.d.	2	52	25	n.d.
Leyou	Angular bitumen (core)	23	2578	13	0,5	n.d.	275	24	3
Leyou	Angular bitumen (halo)	24	9291	184	1485	1230	8528	894	894
Leyou	Angular bitumen (halo)	25	18088	96	1806	427	18582	1721	1721

Tab. 2 Composition of uraninite in FA sandstones determined by EPMA in weight percents of major oxides.

Location	*Point*	*SiO_2*	*P_2O_5*	*CaO*	*TiO_2*	*V_2O_3*	*FeO*	*PbO*	*ThO_2*	*UO_2*	*ZrO_2*	*Total*
Mikouloungou	1	0.91	0	4.32	1.02	0.07	0.57	5.53	0.41	83.23	0.02	96.08
Mikouloungou	2	6.03	0.24	5.1	0.89	0.28	2.1	1.4	0	75.8	0.1	91.94
Mikouloungou	3	0.89	0.07	4.51	1.02	0.16	0.68	4.74	0.12	84.67	0.32	97.18
Mikouloungou	4	0.93	0.12	4.83	1.02	0.21	0.98	4.3	0.27	85.25	0.56	98.47
Mikouloungou	5	1.11	0.04	4.26	1.01	0	0.49	5.84	0	84.93	0.38	98.06
Mikouloungou	6	0.78	0.06	3.97	0.94	0.05	0.64	4.52	0	85.54	0.29	96.79
Mikouloungou	7	7.58	0.22	4.48	2.27	0.09	1.33	2.61	0.07	74.33	0.95	93.93
Mikouloungou	8	1.1	0.07	4.81	1.15	0.07	0.71	4.09	0	84.28	0.18	96.46
Mikouloungou	9	0.92	0.11	4.55	1.15	0.07	0.74	4.43	0.25	83.72	0.09	96.03
Mikouloungou	10	0.84	0.07	4.22	0.93	0.08	0.61	4.73	0.12	84.64	0.2	96.44
Mikouloungou	11	1.2	0.05	4.9	0.61	0.12	1.43	2.03	0	85.43	0.54	96.31
Mikouloungou	12	1.26	0.02	4.21	0.56	0	0.44	5.96	0.01	83.83	0.21	96.5
Mikouloungou	13	1.13	0.2	5.52	0.7	0.29	1.69	0.77	1.28	84.27	0.33	96.18
Mikouloungou	14	1.77	0.22	5.55	0.78	0.28	1.65	0.93	0.03	82.85	0.2	94.26
Mikouloungou	15	1.28	0.02	3.96	0.17	0.05	0.58	5.97	0.15	83.39	0.1	95.67
Mikouloungou	16	1.33	0.03	4.36	0.14	0	0.42	6.22	0.18	84.53	0.11	97.32
Mikouloungou	17	2.14	0.08	5.04	0.51	0.08	1.54	3.32	0	80.04	0.16	92.91
Mikouloungou	18	2.99	0.52	6.87	0.06	0.35	1.53	0.54	0	79.71	0.02	92.59
Mikouloungou	19	4.45	0.04	3.75	0.11	0.11	0.94	4.49	0	76.92	0.4	91.21
Mikouloungou	20	3.24	0.3	3.95	0.07	0.36	0.73	0	0	83.45	1.7	93.8
Mikouloungou	21	2.68	0.24	3.49	0.62	0.42	1.02	0.25	0.19	84.43	2.22	95.56
Mikouloungou	22	3.79	0.07	3.86	0.48	0	0.49	5.04	0	80.87	0.28	94.88
Mikouloungou	23	1.79	0	3.81	0.71	0.09	0.41	5.34	0	82.85	0.46	95.46
Mikouloungou	24	2.87	0.45	2.69	0	0.29	0.83	1.62	0	85.5	0.15	94.4
Mikouloungou	25	3.75	0.19	2.51	0	0.04	0.88	2.82	0	83.54	0.28	94.01
Mikouloungou	26	3.59	0.41	3.46	0	0.11	0.84	1.89	0	83.12	0.29	93.71
Mikouloungou	27	3.75	1.3	2.18	0	0.15	0.65	2.81	0	79.33	0.68	90.85
Mikouloungou	28	2.58	0.31	3.42	0	0.21	1	1.44	0	86.76	0.15	95.87
Mikouloungou	29	2.56	0.34	3.22	0.02	0.27	0.94	1.07	0	84.62	0.52	93.56
Mikouloungou	30	5.75	0.25	5.99	0	0.15	0.08	1.3	0	84.28	0.37	98.17
Mikouloungou	31	4.78	0.26	5.42	0.29	0.42	0.26	1.6	0	82.51	0	95.54
Mikouloungou	32	1	0.13	5.15	0	0.53	0.91	3.09	0	85.81	0.18	96.8
Mikouloungou	33	1.06	0.17	4.96	0.12	0.5	0.79	3.01	0	85.81	0.42	96.84
Mikouloungou	34	1.92	0.16	4.37	0.36	0.28	0.81	2.93	0	85.8	0.44	97.07
Mikouloungou	35	0.8	0.01	4.53	0.31	0.09	0.65	3.89	0	84.67	0.31	95.26
Mikouloungou	36	6.38	0.38	4.32	0.1	0.51	0.69	1.7	0	74.87	0.25	89.2
Mikouloungou	37	4.7	0.38	5.04	0	0.48	0	1.49	0	80.24	1.1	93.43
Mikouloungou	38	8.16	0.47	4.53	0.19	0.37	0.01	0.98	0	73.26	0.7	88.67
Mikouloungou	39	1.49	0.08	4.36	0.75	0.23	0.69	2.64	0.19	84.61	0.58	95.62
Mikouloungou	40	4.84	0.38	4.65	0.63	0.54	0.85	1.15	0	76.81	0.31	90.16
Mikouloungou	41	3.26	0.17	5.19	0.5	0.4	1.06	0.37	0.02	86.64	0.51	98.12
Mikouloungou	42	1.6	0.07	4.52	0	0.17	0.46	5.84	0	83.22	0.92	96.8
Okélobondo	43	1.62	0.13	2.93	1.32	0.41	0.46	0.83	0.36	88.78	0.15	96.99
Okélobondo	44	2.57	0.18	2.54	1.3	0.27	0.3	1.03	0	86.48	0.23	94.9
Okélobondo	45	5.63	0.26	1.67	0.59	0.29	0.49	0.5	0	79.21	0	88.64
Okélobondo	46	0.78	0	2.9	0.54	0.04	0.59	5.36	0	87.69	0	97.9
Okélobondo	47	1.04	0.05	2.7	0.72	0.02	0.5	3.69	0	87.73	0.19	96.64
Okélobondo	48	1.04	0.05	3.01	0.71	0.04	0.47	5.58	0.01	87.91	0	98.82
Okélobondo	49	1.02	0.09	2.55	0.74	0.04	0.57	3.33	0.05	89.48	0.25	98.12
Okélobondo	50	1.48	0.02	2.94	0.28	0.08	0.42	4.78	0	86.95	0.17	97.12
Okélobondo	51	0.93	0.02	3.06	0.3	0.04	0.45	6.21	0	87.26	0	98.27
Okélobondo	52	1.47	0.14	2.24	1.05	0	0.84	4.68	0	87.04	0	97.46
Okélobondo	53	0.66	0.13	2.48	0.18	0.04	0.46	6.4	0.08	85.85	0.14	96.42
Okélobondo	54	6.69	0.19	2.82	0.4	0.08	2.01	0.8	0.21	83.67	0	96.87
Okélobondo	55	1.92	0.25	3.11	0.44	0.14	1.03	2.98	0	85.85	0	95.72
Okélobondo	56	3.01	0.27	2.73	0.4	0.02	1.2	1.98	0.01	85.68	0.1	95.4
Okélobondo	57	0.88	0.11	2.24	0.8	0	0.54	4.05	0.04	87.66	0	96.32
Bangombé	58	0.43	1.03	1.42	1.2	0	0.92	5.13	0	83.51	0.12	93.76
Bangombé	59	1.02	0.13	1.72	0.49	0.09	0.94	5.71	0	85.8	0.23	96.13

Tab. 3 Rare Earth Element concentrations in FA uraninites (ppm) from LA-ICP-MS analysis.

Location	*Point*	*Y ppm*	*La ppm*	*Ce ppm*	*Pr ppm*	*Nd ppm*	*Sm ppm*	*Eu ppm*	*Gd ppm*	*Tb ppm*	*Dy ppm*	*Ho ppm*	*Er ppm*	*Tm ppm*	*Yb ppm*	*Lu ppm*
Mikou.	1	2124	712	3512	621	3460	857	230	820	71	291	47	87	7	32	4
Mikou.	2	2768	945	4333	684	3425	823	296	922	73	301	46	86	6	33	4
Mikou.	3	1431	1141	4424	700	2999	654	280	607	45	177	24	48	3	17	2
Mikou.	4	1980	959	4299	710	3676	798	313	774	66	267	43	82	6	29	4
Mikou.	5	1195	834	3252	497	2450	540	189	495	43	178	28	51	4	19	3
Mikou.	6	1567	863	3703	569	2887	674	297	628	55	224	35	68	5	25	3
Oklo	7	176	176	1722	300	1334	253	102	175	16	62	8	17	1	8	0.8
Oklo	8	137	292	1863	254	990	190	61	132	13	52	7	14	1	7	0.8
Oklo	9	130	264	1592	219	847	162	51	112	11	44	6	12	1	6	0.7
Oklo	10	181	261	1484	209	804	175	54	144	14	57	8	16	2	7	0.9
Oklo	11	368	270	1867	274	1152	263	84	240	24	95	13	28	2	12	2
Oklo	12	203	233	1504	265	1213	263	84	181	16	65	9	17	2	8	0.9
Okélo.	13	192	8	174	60	345	206	68	178	16	56	6	10	0.9	5	0.5
Okélo.	14	179	21	387	126	623	244	47	176	19	69	7	11	1	7	0.5
Okélo.	15	198	9	137	44	283	300	54	221	24	85	8	15	1	9	0.8
Okélo.	16	193	14	294	96	521	296	47	230	20	85	6	14	0.8	10	0.7
Okélo.	17	176	9	207	70	373	256	43	194	20	75	8	13	1	8	0.7
Okélo.	18	214	7	148	50	308	202	60	199	18	59	6	10	1	5	0.5
Okélo.	19	160	11	249	84	423	177	45	158	15	54	5	9	0.9	6	0.5
Okélo.	20	175	11	214	60	327	247	50	190	19	68	7	12	1	8	0.7
Okélo.	21	218	7	164	52	304	211	62	208	20	70	7	11	1	6	0.6
Okélo.	22	194	10	186	61	333	220	57	188	18	63	7	11	1	6	0.6
Okélo.	23	177	11	221	68	364	200	56	177	18	63	6	11	1	5	0.7
Okélo.	24	127	14	272	98	506	180	40	129	13	46	5	9	0.9	5	0.6
Mikou.	25	1854	765	2390	357	1732	660	57	673	80	378	59	118	9	46	7
Mikou.	26	747	531	1760	260	1318	361	36	297	32	147	21	42	3	18	2
Mikou.	27	1621	736	2843	464	2296	637	108	596	63	272	42	82	7	32	4
Mikou.	28	629	495	1345	173	744	255	14	226	27	130	20	39	3	17	2
Okélo.	29	63	28	434	137	606	133	18	66	7	29	3	6	0.6	5	0.5
Okélo.	30	73	23	370	122	568	139	22	77	8	31	3	6	0.7	4	0.5
Okélo.	31	133	35	502	149	658	177	15	109	12	47	5	11	1	7	0.8
Okélo.	32	152	44	654	199	893	200	16	122	14	52	6	12	1	9	1
Okélo.	33	101	28	386	114	469	138	30	101	10	35	3	6	0.6	3	0.5
Okélo.	34	30	72	336	49	189	46	3	30	3	15	2	4	0.3	2	0.3
Okélo.	35	24	72	312	42	157	39	2	23	3	10	2	3	0.3	2	0.3
Okélo.	36	45	41	294	52	232	65	4	44	5	26	3	7	0.9	5	0.5
Okélo.	37	33	60	338	51	211	51	3	33	4	16	2	4	0.4	3	0.4
Okélo.	38	51	71	387	58	236	67	4	49	6	29	4	8	0.8	6	0.5
Okélo.	39	97	101	476	70	315	105	5	83	10	45	7	13	1	8	0.7
Okélo.	40	32	55	319	50	207	52	3	33	4	16	2	4	0.5	3	0.3
Okélo.	41	40	42	317	52	225	60	3	40	5	20	3	6	0.6	4	0.4
Okélo.	42	36	78	349	48	201	49	3	35	4	16	2	4	0.5	3	0.3
Okélo.	43	44	45	356	57	235	64	4	47	5	21	3	5	0.5	3	0.4
Okélo.	44	40	40	307	53	228	60	3	39	5	22	3	6	0.5	3	0.3
Okélo.	45	32	61	328	47	188	46	3	30	4	15	2	5	0.4	2	0.2
Okélo.	46	28	51	306	47	187	46	3	28	3	14	2	4	0.5	3	0.2
Okélo.	47	54	54	363	60	257	68	5	48	5	24	3	7	0.7	4	0.4
Okélo.	48	42	62	388	61	249	65	4	43	5	21	3	5	0.6	3	0.4
Okélo.	49	50	50	338	56	240	66	4	45	5	22	3	6	0.6	4	0.5
Okélo.	50	34	56	275	41	168	44	3	33	4	17	2	5	0.4	3	0.3
Okélo.	51	68	31	317	58	269	75	5	58	7	26	4	8	0.9	5	0.6
Okélo.	52	59	31	295	52	240	74	4	53	6	29	4	8	0.8	5	0.5
Bangombé	53	1103	584	1360	136	508	87	22	136	12	67	15	43	5	28	5
Bangombé	54	365	574	1119	100	316	40	9	53	5	26	5	14	1	9	2
Mikou.	55	9	360	354	31	79	12	7	4	1	5	0.9	3	0.4	3	0.3
Mikou.	56	31	459	441	38	102	12	8	7	1	6	1	3	0.5	4	0.4
Mikou.	57	16	345	328	27	83	12	7	5	0.9	5	0.9	3	0.4	3	0.3

Tab. 4 Composition of Fe-chlorites determined by EPMA.

Location	*Point*	*Na_2O*	*MgO*	*Al_2O_3*	*SiO_2*	*K_2O*	*CaO*	*TiO_2*	*MnO_2*	*V_2O_3*	*FeO*	*Total*	*T (°C)*
Mikou.	1	0.01	6.98	22.04	25.32	0.01	0.05	0	0.22	0.25	27.92	82.81	154
Mikou.	2	0.02	7.71	22.47	24.87	0.02	0.12	0	0.14	0.43	29	84.79	196
Mikou.	3	0.02	7.41	21.5	25.28	0	0.03	0	0.06	0.24	27.79	82.33	156
Mikou.	4	0	9.94	21.68	24.14	0.1	0.01	0.03	0	0.67	26.72	83.29	257
Mikou.	5	0.05	9.46	21.28	24.56	0.01	0.02	0	0.13	1.13	25.93	82.54	230
Mikou.	6	0	6.8	22.89	24.24	0.03	0.04	0.01	0.09	0.65	27.43	82.19	180
Bangombé	7	0.02	9.26	23.61	25.08	0.03	0.04	0	0.14	0	26.01	84.17	178
Bangombé	8	0.02	10.62	23.85	24.41	0	0.01	0	0.12	0	25.19	84.23	216
Bangombé	9	0	10.3	23.65	25.19	0.03	0	0	0.1	0.04	24.31	83.62	177
Bangombé	10	0.02	9.23	24.07	23.06	0	0	0.01	0.11	0	25.71	82.22	230
Bangombé	11	0.01	8.99	23.38	24.5	0.02	0.04	0	0.14	0.02	26.65	83.74	193
Bangombé	12	0	10.27	22.9	23.88	0	0	0.01	0.14	0.04	25.31	82.55	223
Bangombé	13	0.02	10.27	22.66	23.76	0.01	0	0	0.06	0.03	26.1	82.91	241
Bangombé	14	0.09	6.86	22	23.46	0.02	0.01	0	0.12	0	29.58	82.15	205
Bangombé	15	0	8.06	22.74	23.81	0	0.01	0	0.22	0.04	28.66	83.55	217
Bangombé	16	0.04	6.28	21.47	24.72	0.07	0.08	0	0.12	0.04	29.27	82.07	158
Bangombé	17	0.01	7.82	22.05	24.26	0	0	0.02	0.16	0.06	28.82	83.2	196
Bangombé	18	0.14	8.05	22.17	23.76	0.03	0.02	0.01	0	0.02	28.87	83.07	220
Bangombé	19	0.05	7.25	21.52	23.94	0.03	0.05	0	0.09	0	29.5	82.43	198
Bangombé	20	0.01	6.81	22.19	23.3	0.02	0.03	0.02	0.1	0.08	30.2	82.76	221
Bangombé	21	0.03	6.88	21.72	23.7	0	0.04	0	0.14	0.07	30.71	83.3	217
Bangombé	22	0	8.2	23.04	24.53	0.03	0.1	0	0.12	0	26.56	82.58	174
Bangombé	23	0.04	7.92	24.2	24	0.09	0.03	0	0.19	0.02	27.38	83.86	197
Bangombé	24	0	9.1	22.78	24.19	0.03	0	0	0.16	0.02	26.62	82.91	201
Bangombé	25	0.03	7.85	24.14	24.36	0.01	0.06	0.02	0.02	0	27.89	84.38	188
Bangombé	26	0.01	8.26	23.55	23.77	0	0.05	0	0	0.03	28.24	83.91	216
Bangombé	27	0	8.02	24.02	23.54	0.01	0	0.01	0.13	0.04	29.1	84.86	236
Bangombé	28	0.01	8.08	23.62	24.39	0.02	0.06	0	0.05	0	28.01	84.25	192
Bangombé	29	0.03	7.75	23.47	23.8	0.04	0.09	0	0.14	0.02	26.85	82.19	188
Bangombé	30	0.05	9.41	23.12	24.06	0	0	0	0.17	0	27.43	84.25	228
Okélo.	31	0.05	8.52	22.45	24.77	0.01	0	0.06	0.02	1.31	27.28	84.46	225
Okélo.	32	0	9.52	22.67	24.65	0.01	0.09	0.02	0	0.94	25.52	83.42	214
Okélo.	33	0.03	10.06	23.2	23.82	0	0.05	0.02	0.09	1.02	26.26	84.56	300
Okélo.	34	0	9.07	21.77	23.47	0	0.02	0	0.18	1.4	27.21	83.12	334
Okélo.	35	0	7.29	21.47	23.41	0	0.01	0.01	0.07	2.14	28.97	83.37	317
Okélo.	36	0	9.65	22.07	24.07	0	0.03	0	0.16	1.14	26.84	83.96	287
Okélo.	37	0.02	10.29	21.85	24.01	0	0.02	0	0.07	1.14	26.07	83.46	302
Okélo.	38	0.02	5.77	21.22	23.2	0	0.06	0.01	0.15	2.28	31.18	83.88	330

Fig. 1. General geological map of Gabon with main palaeoproterozoic basins (adapted from Préat *et al.*, 2011).

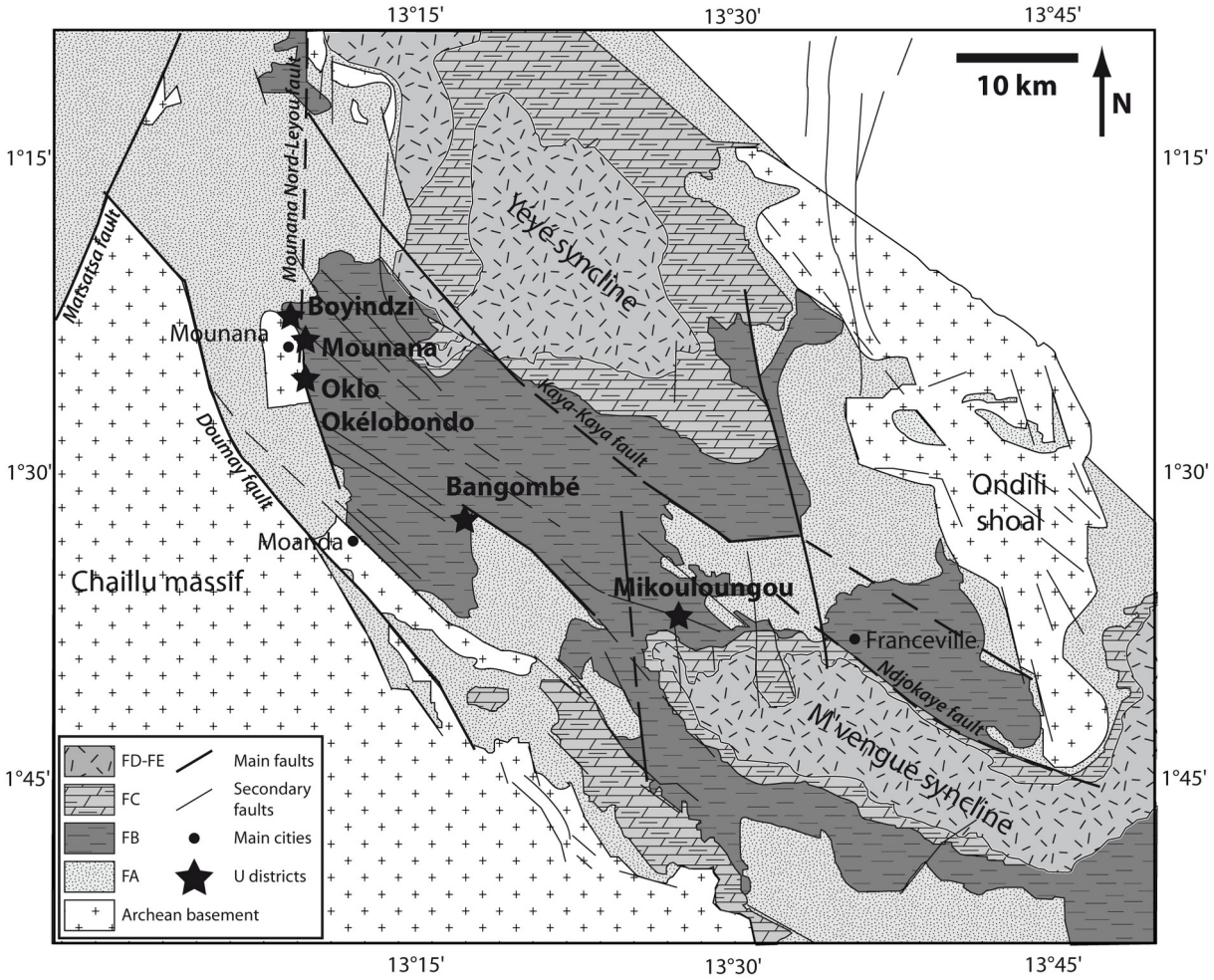

Fig. 2. Geological map of Franceville basin with main uranium districts (adapted from Ossa Ossa *et al.*, 2014).

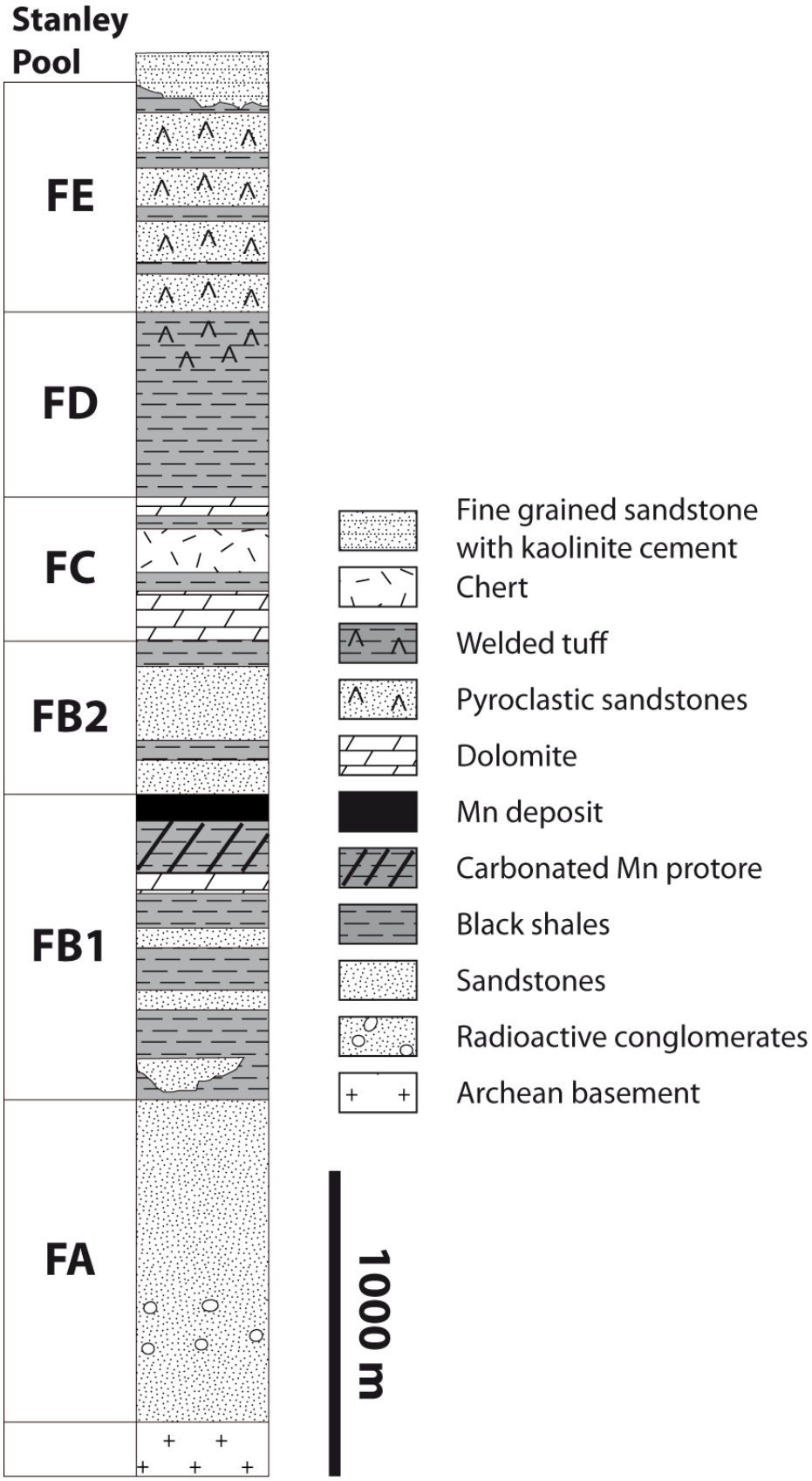

Fig. 3. Stratigraphic column of the Francevillian Series in the Franceville basin (adapted from Gauthier-Lafaye and Weber, 2003). FA, FB, FC, FD and FE formations are described in the text.

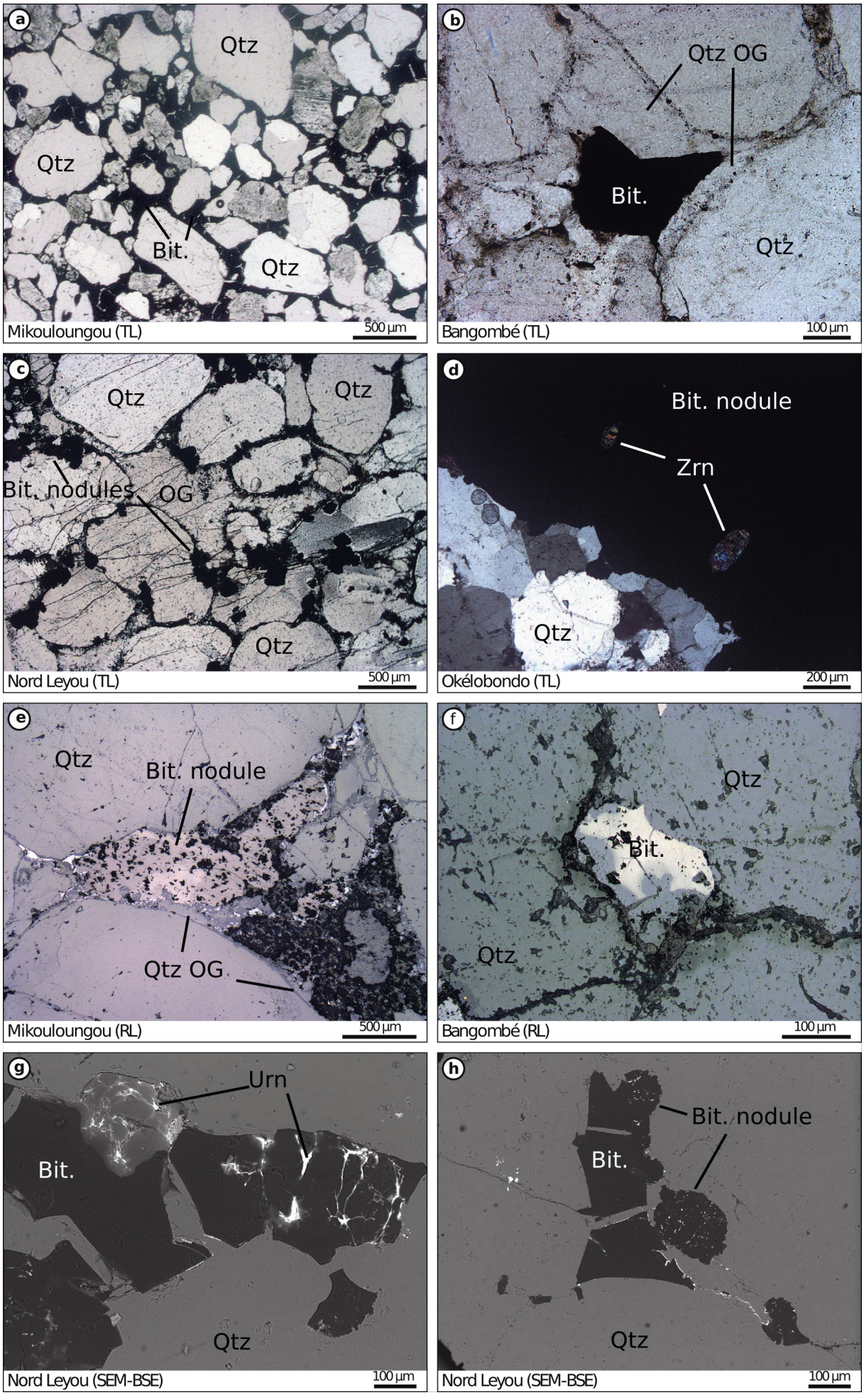
a
Qtz
Qtz
Bit.
Qtz
Mikouloungou (TL)
500 µm
b
Qtz OG
Bit.
Qtz
Bangombé (TL)
100 µm
c
Qtz
Qtz
Bit. nodules
OG
Qtz
Nord Leyou (TL)
500 µm
d
Bit. nodule
Zrn
Qtz
Okélobondo (TL)
200 µm
e
Qtz
Bit. nodule
Qtz OG
Mikouloungou (RL)
500 µm
f
Qtz
Bit.
Qtz
Bangombé (RL)
100 µm
g
Urn
Bit.
Qtz
Nord Leyou (SEM-BSE)
100 µm
h
Bit. nodule
Bit.
Qtz
Nord Leyou (SEM-BSE)
100 µm

Fig. 4. Petrographic features of organic matter in FA sandstones (TL: transmitted light; RL: reflected light). **a.** Bitumen cemented sandstone. **b.** Quartz overgrowths (OG) and bitumen (Bit.) filling residual porosity. **c.** Bitumen nodules on the contact between detrital quartz and overgrowths. **d.** Massive bitumen nodule crosscutting detrital quartz with preserved refractory zircons (Zrn). **e.** Bitumen nodule and partially dissolved quartz overgrowths. **f.** Low reflectance halo on a bitumen nodule. **g.** Low reflectance halo observed with SEM-BSE. **h.** Rare occurrence of coexisting angular bitumen and nodules.

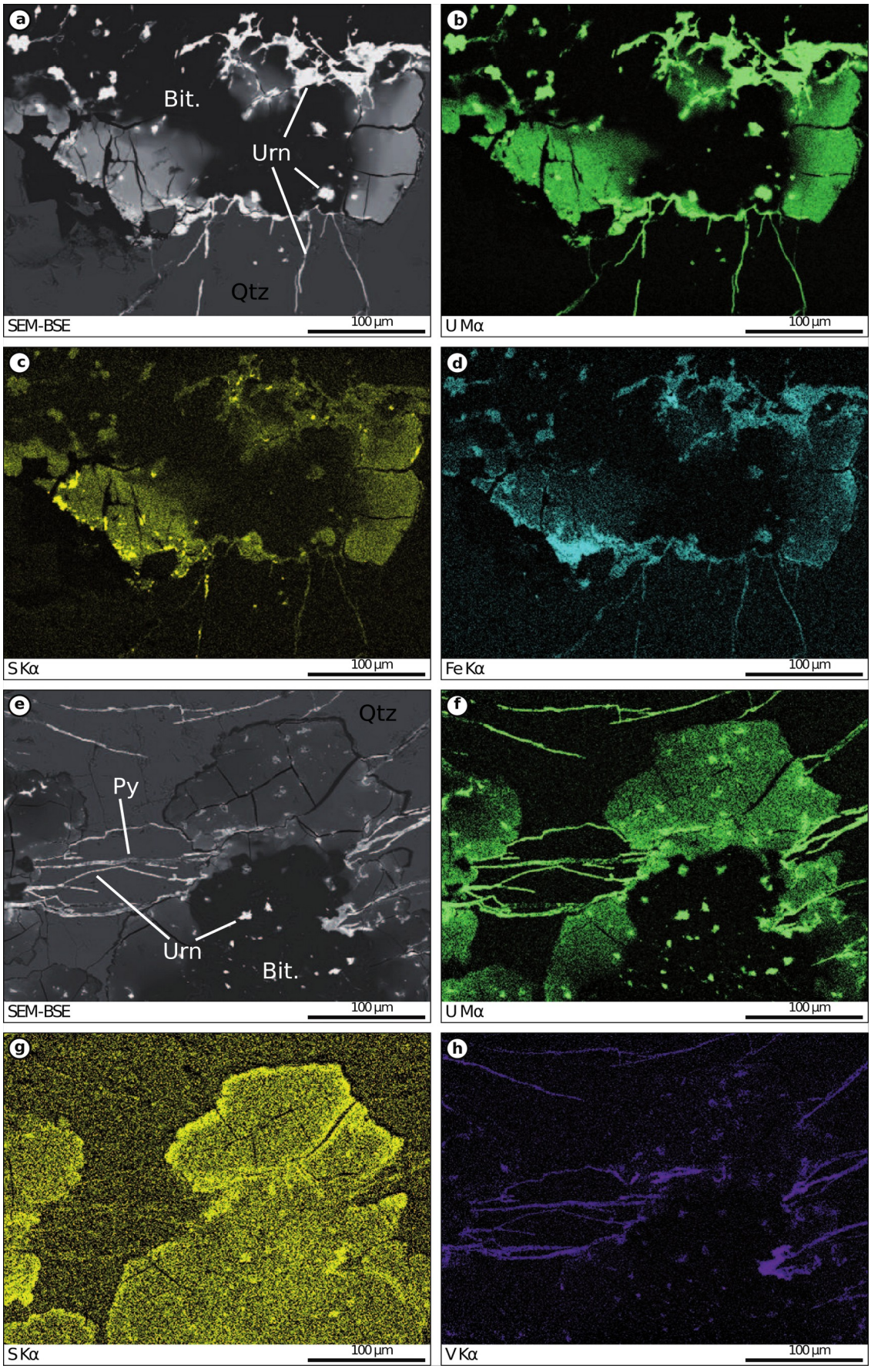

Fig. 5. U, S, Fe and V X-ray maps of bitumen nodules with low reflectance halos.

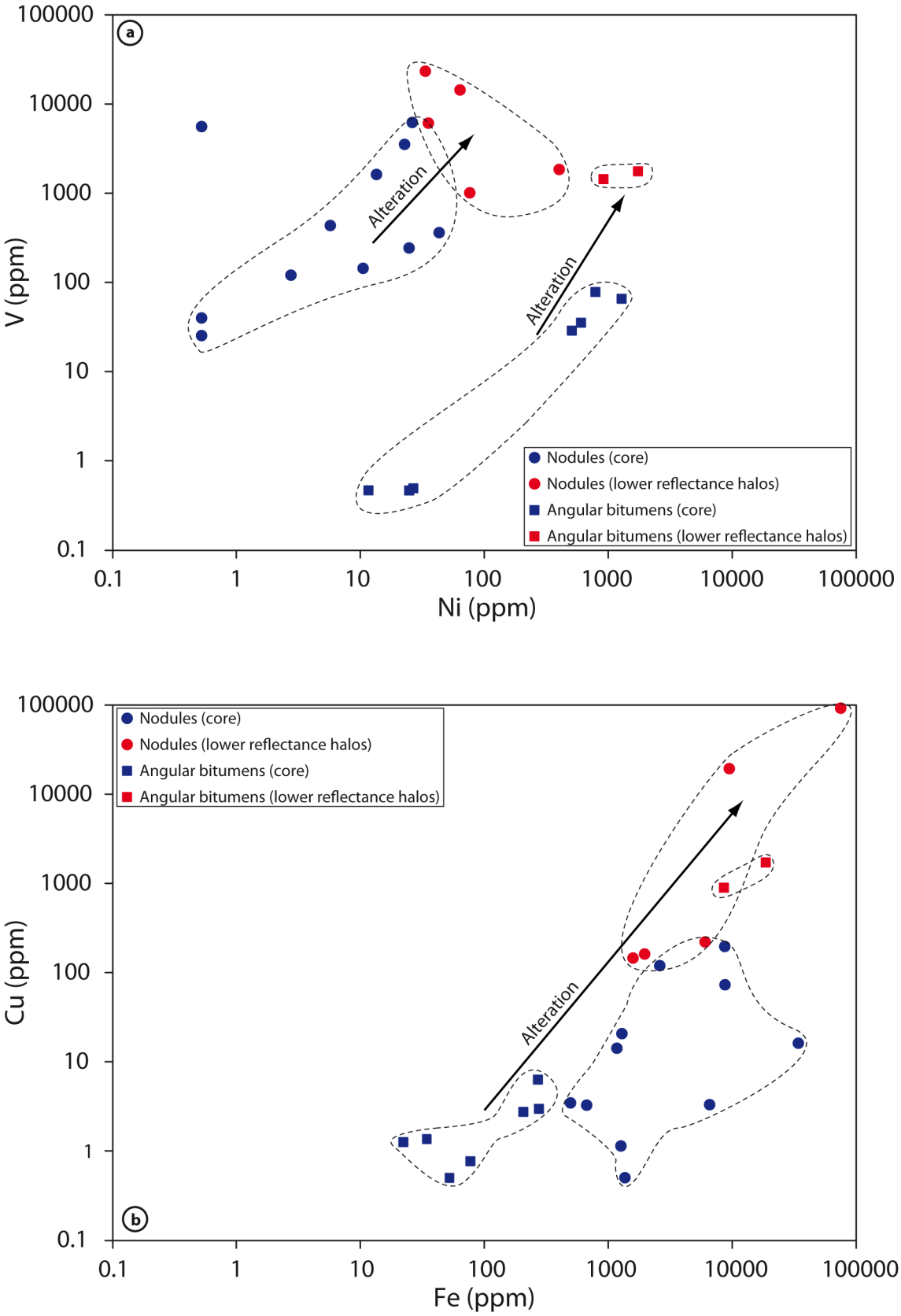

Fig. 6. V-Ni and Cu-Fe diagrams of angular bitumens and nodules in FA sandstones (LA-ICP-MS analyses).

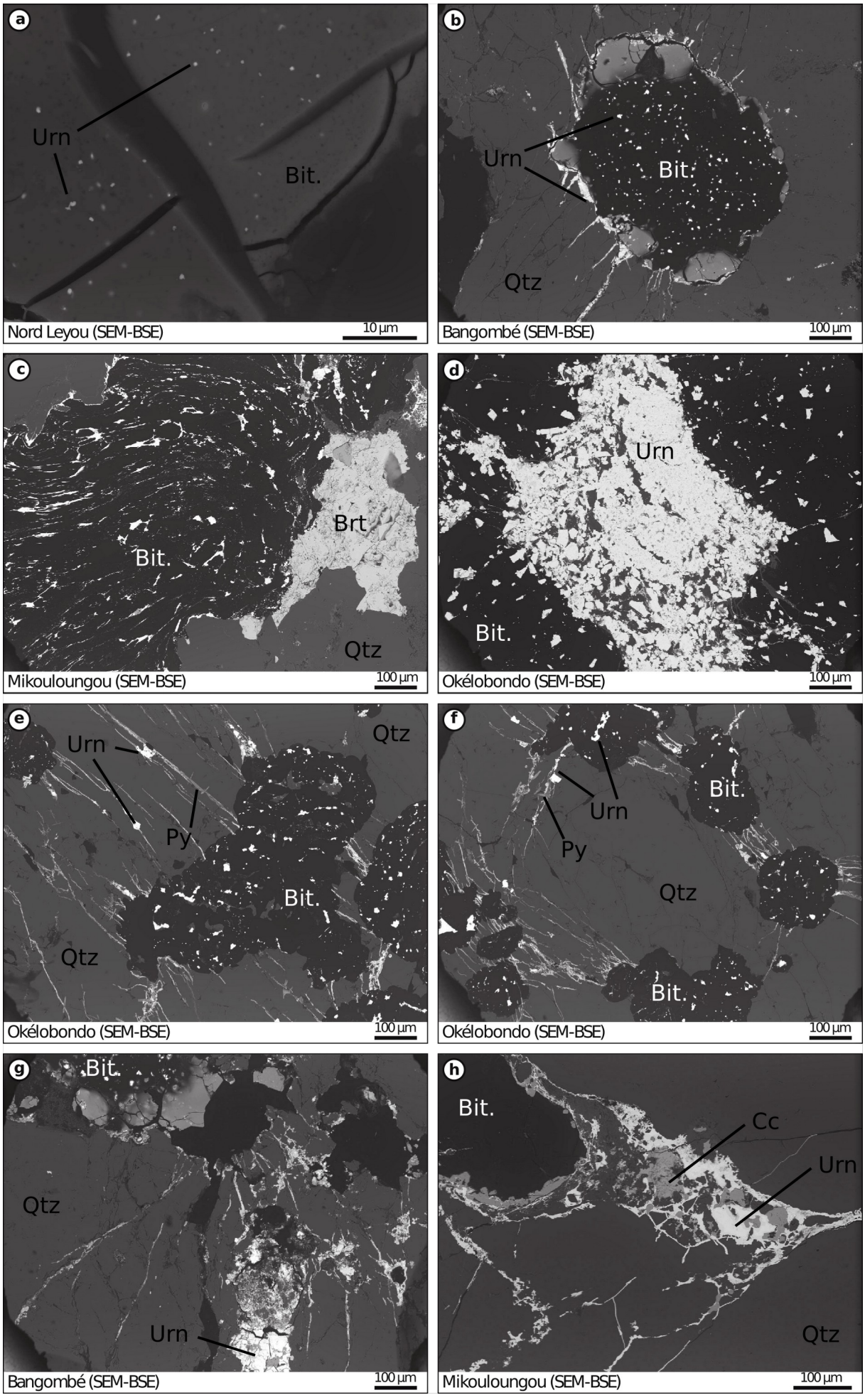
a
Urn
Bit.
Nord Leyou (SEM-BSE)
10 µm
b
Urn
Bit.
Qtz
Bangombé (SEM-BSE)
100 µm
c
Brt
Bit.
Qtz
Mikouloungou (SEM-BSE)
100 µm
d
Urn
Bit.
Okélobondo (SEM-BSE)
100 µm
e
Urn
Qtz
Py
Bit.
Qtz
Okélobondo (SEM-BSE)
100 µm
f
Bit.
Urn
Py
Qtz
Bit.
Okélobondo (SEM-BSE)
100 µm
g
Bit.
Qtz
Urn
Bangombé (SEM-BSE)
100 µm
h
Bit.
Cc
Urn
Qtz
Mikouloungou (SEM-BSE)
100 µm

Fig. 7. Petrographic features of association between organic matter (black), uranium (Urn, white) and sulfides in FA sandstones. **a.** U nano-inclusions in bitumen nodule. **b.** Bitumen nodule with UO_2 inclusions, low reflectance rim and radial U-filled fractures. **c.** Bitumen nodule with elongated UO_2 inclusions and barite (Brt). **d.** Large UO_2 and UO_2 crystals in the center of a bitumen nodule. Residual porosity is filled by quartz (gray). **e.** Bitumen nodules and fractures filled by UO_2 and sulfides (mainly pyrite, Py). **f.** Circular fracture network (UO_2 and pyrite) connecting bitumen nodules **g.** Bitumen nodule with UO_2 inclusions, low reflectance rim and U-filled fractures (sulfides are pyrite and chalcopyrite). **h.** Bitumen with fractures filled by UO_2 and chalcocite (Cc).

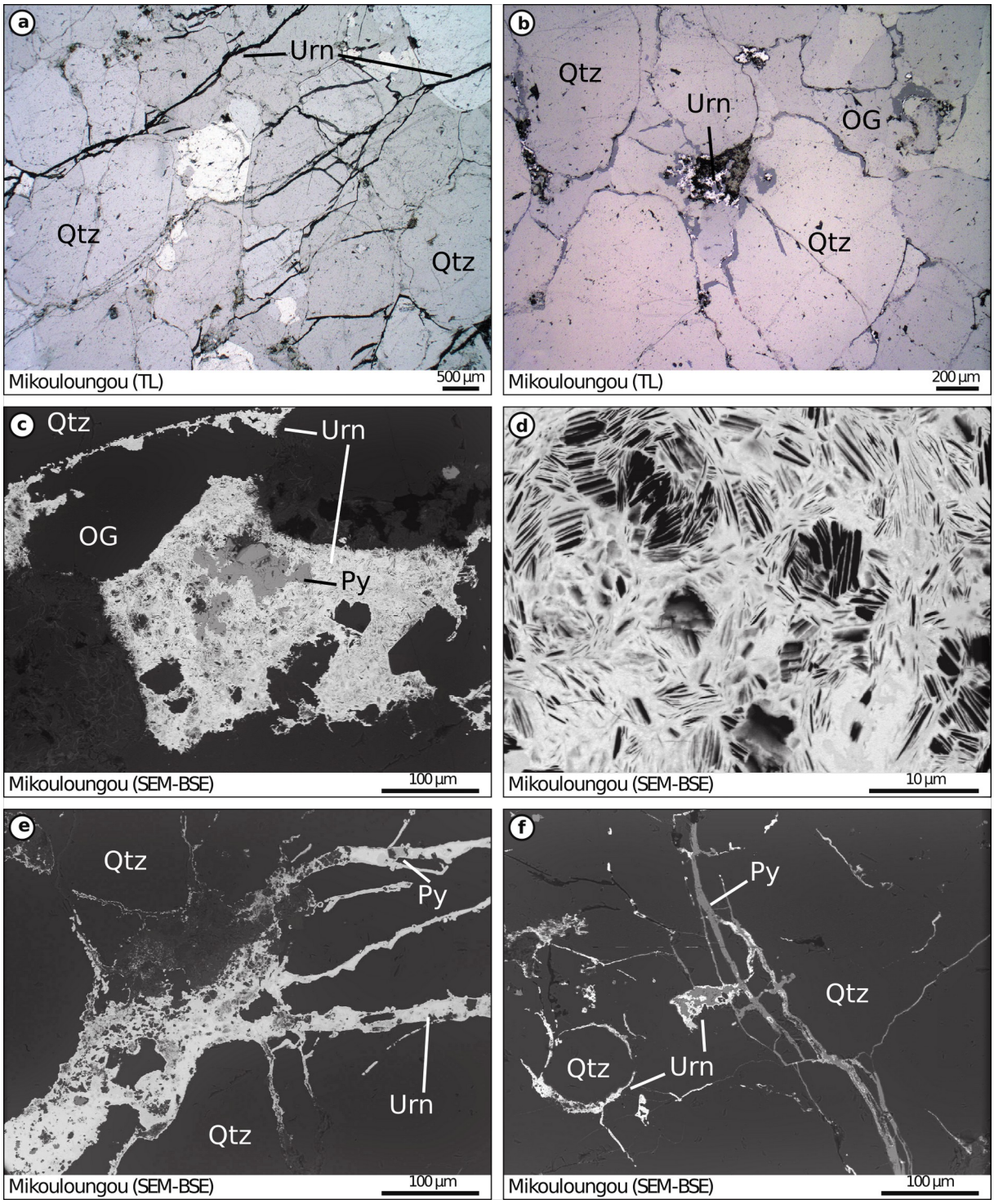

Fig. 8. Petrographic features of fractures in FA sandstones. **a.** Fracture network crosscutting detrital quartz (Qtz) and overgrowths (OG). **b.** Fractures and UO_2 precipitation at the boundary between detrital quartz and overgrowths. **c.** UO_2 precipitation on clays and at the boundary between detrital quartz and overgrowths. **d.** Detail of UO_2 and illites. **e.** Fractures filled by UO_2 and pyrite. **f.** Fractures filled by UO_2 and pyrite.

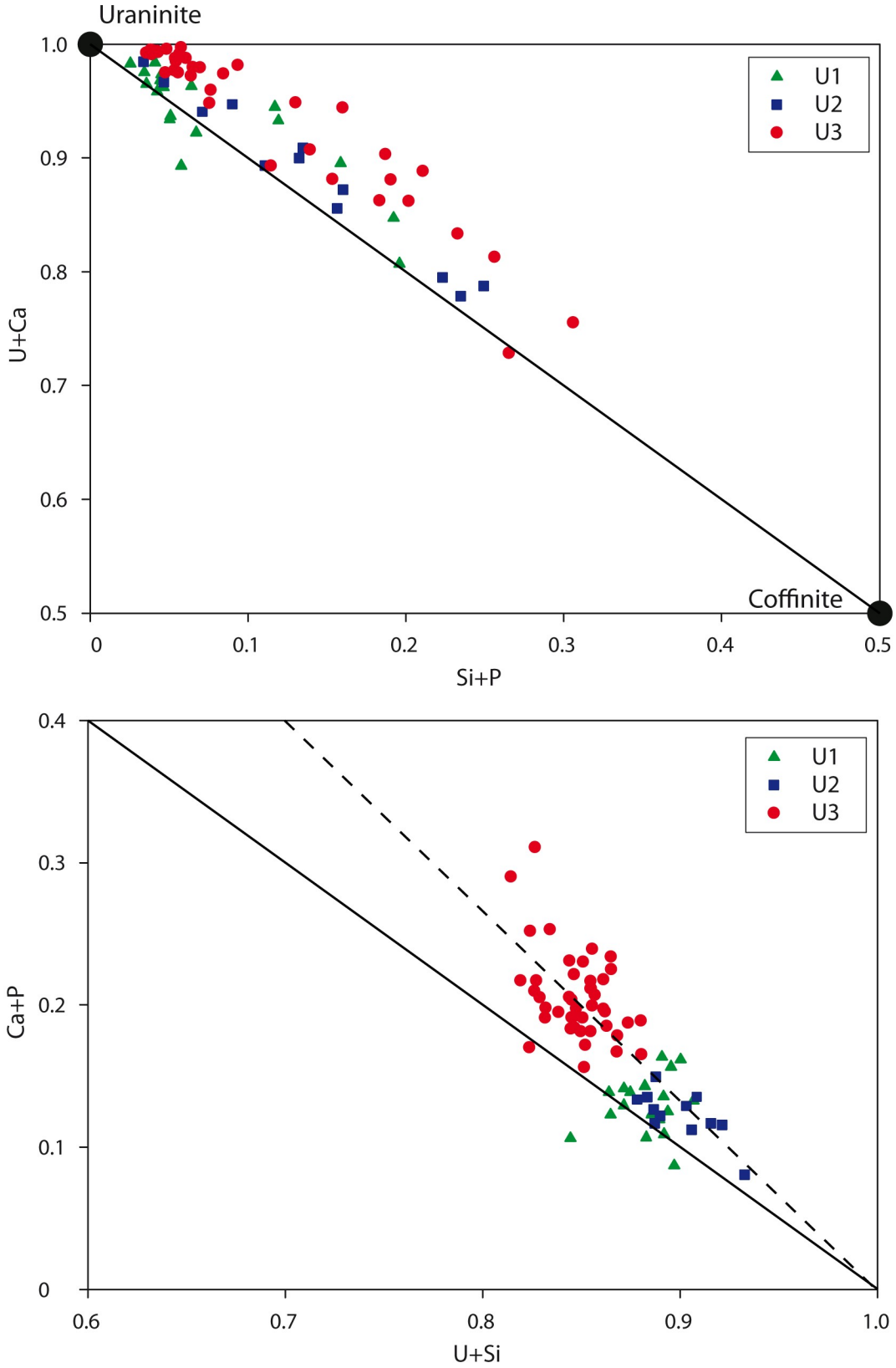

Fig. 9. U+Ca vs Si+P and Ca+P vs U+Si diagrams of uranium mineralization in FA sandstones (APFU Atoms Per Formula Unit). U1, U2 and U3 are represented by triangles, squares and circles, respectively.

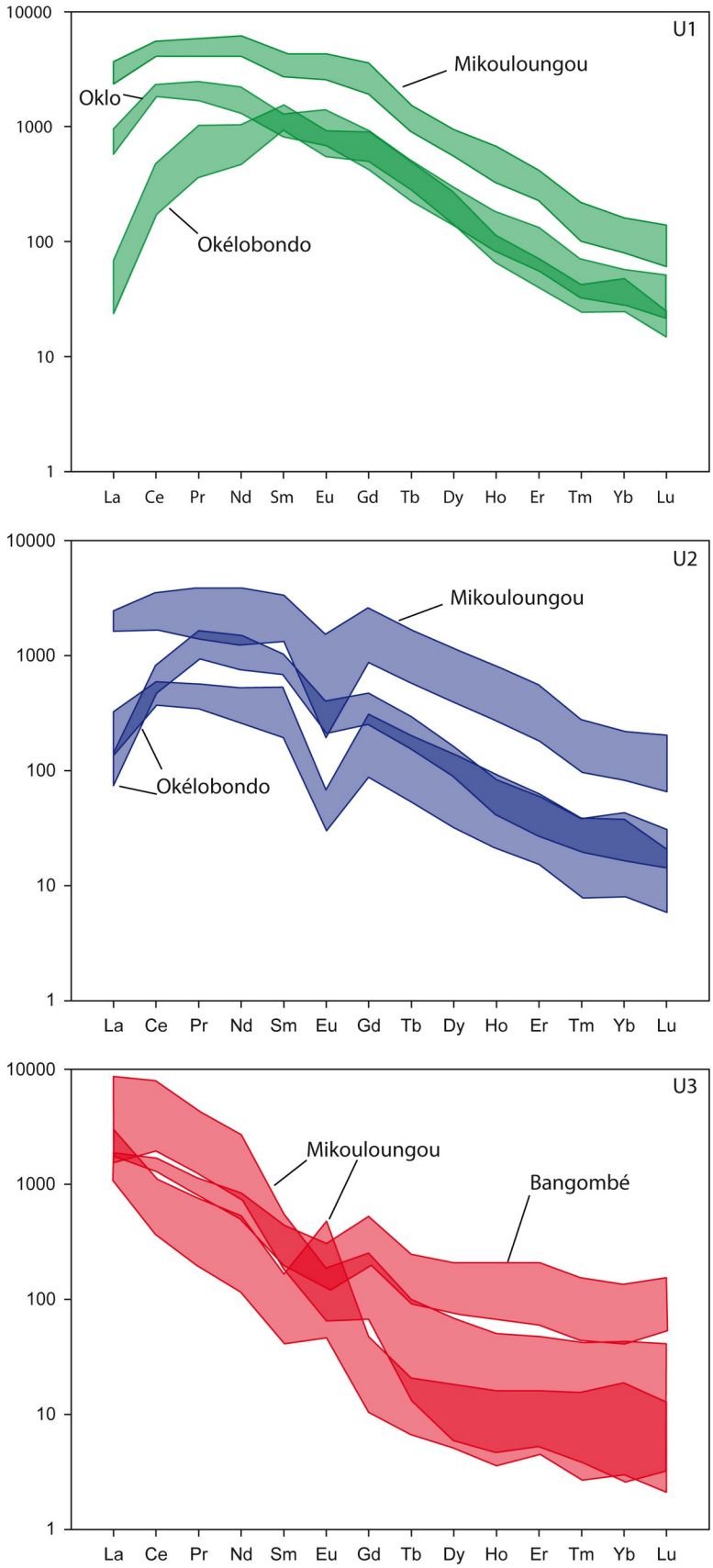

Fig. 10. REE patterns in U1, U2 and U3 uraninites from Mikouloungou, Bangombé and Oklo-Okélobondo locations.

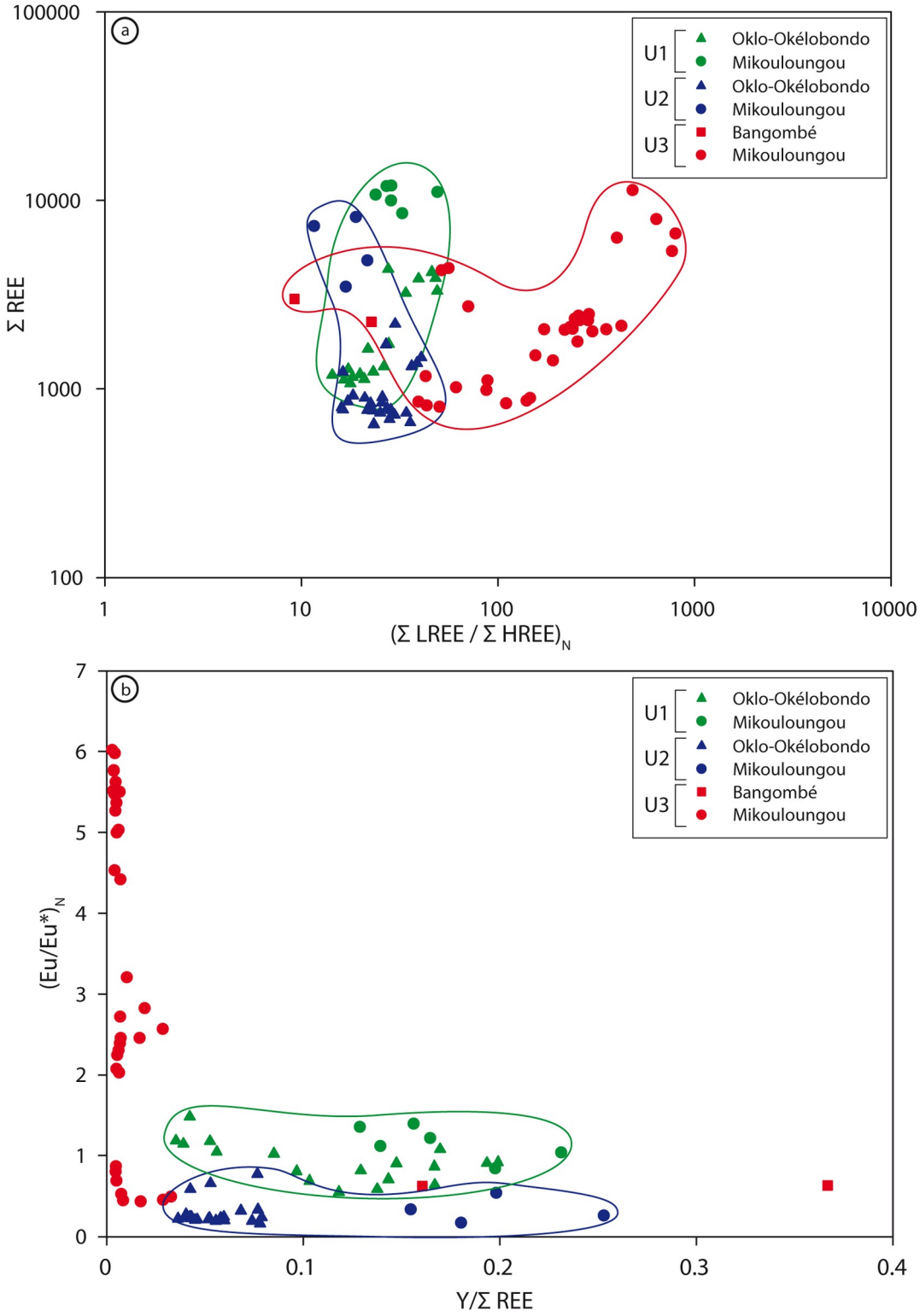

Fig. 11. Σ REE vs $(\Sigma \text{ LREE} / \Sigma \text{ HREE})_N$ and Eu/Eu* vs Y/Σ REE diagrams in U1, U2 and U3 uraninites from Mikouloungou, Bangombé and Oklo-Okélobondo locations.

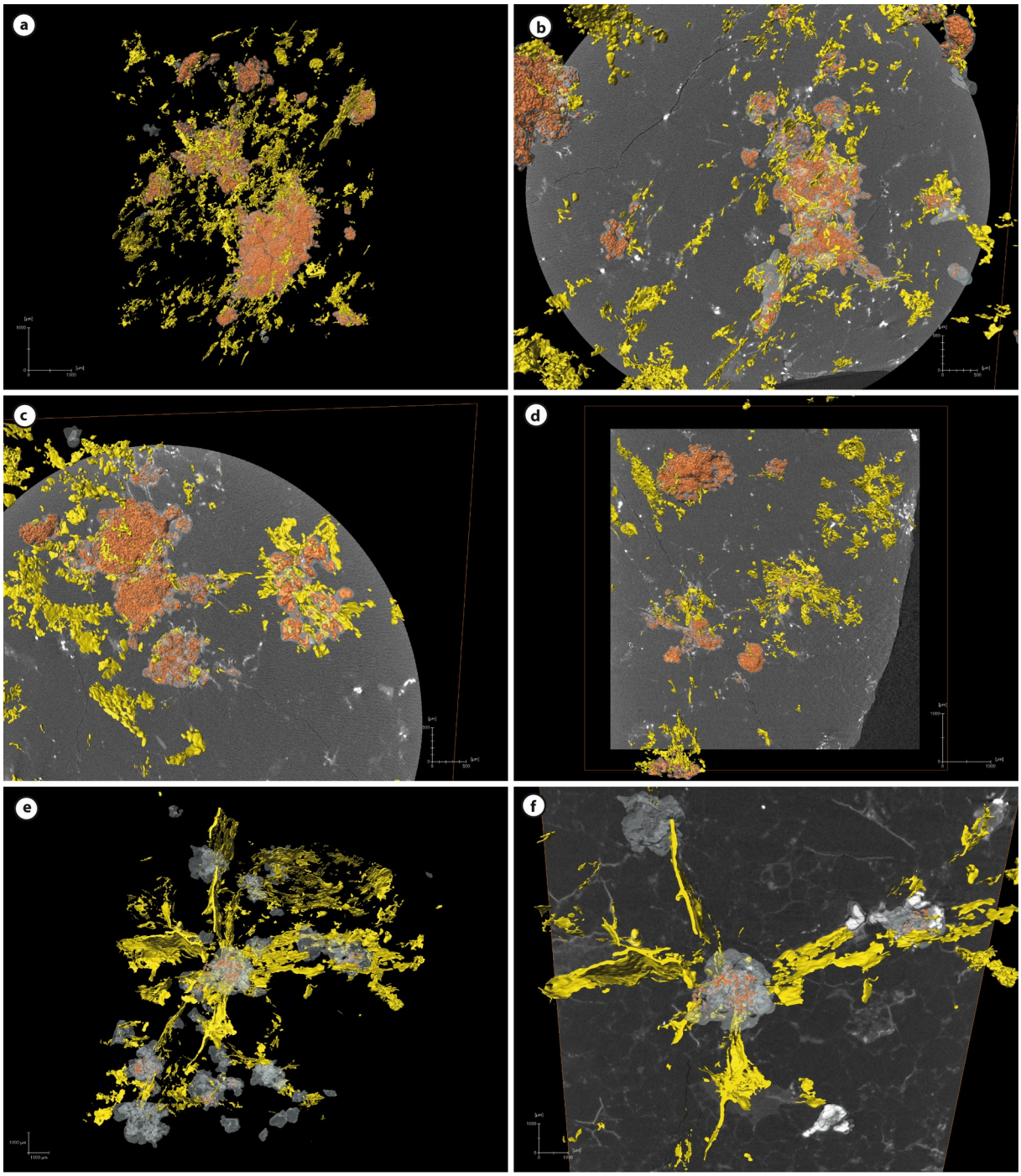

Fig. 12. 3D views from X-ray tomography on samples from Okélobondo (a to d) and Bangombé (e and f). U1-U2 are in orange, U3 in yellow and bitumen nodules are in transparent white. One video of 3D reconstruction can be downloaded from supplementary materials.

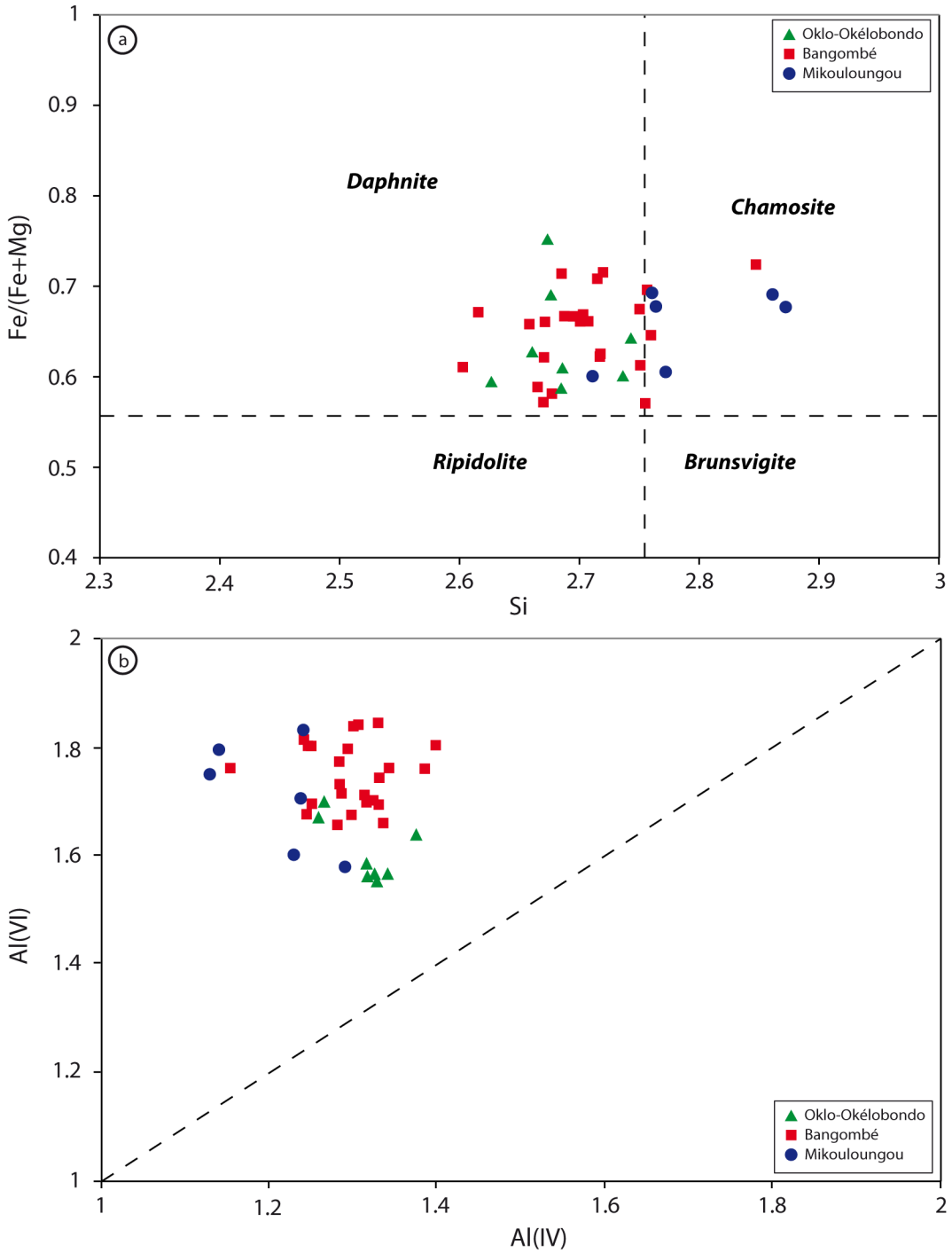

Fig. 13. Fe/(Fe+Mg) vs Si and Al(VI) vs Al(IV) diagrams for Fe-chlorites in Oklo-Okélobondo (green triangles), Bangombé (red squares) and Mikouloungou (blue dots) samples.

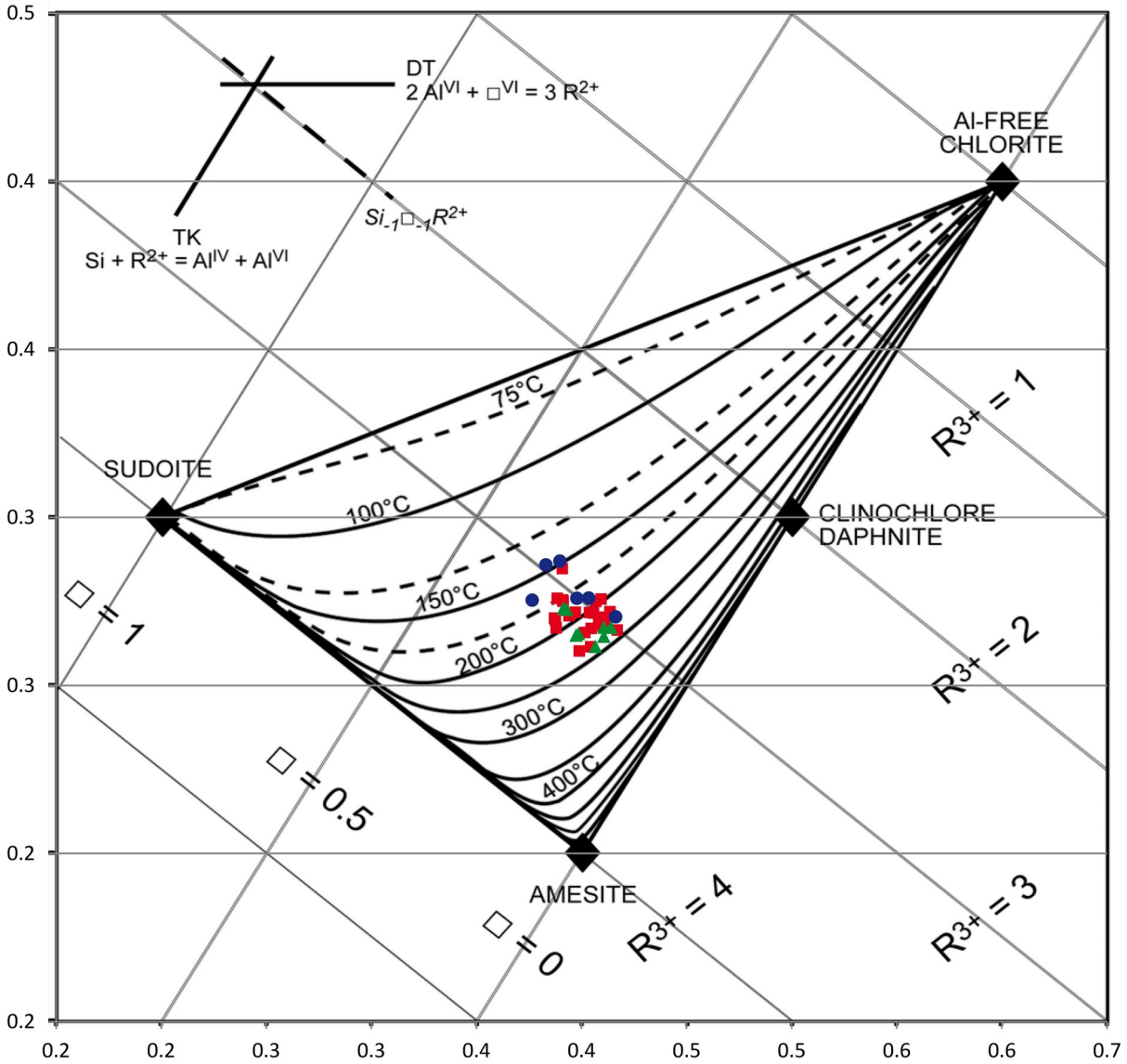

Fig. 14. Si vs R^{2+} diagram (Bourdelle & Cathelineau, 2015) for Fe-chlorites in Oklo-Okélobondo (green triangles), Bangombé (red squares) and Mikouloungou (blue dots) samples.

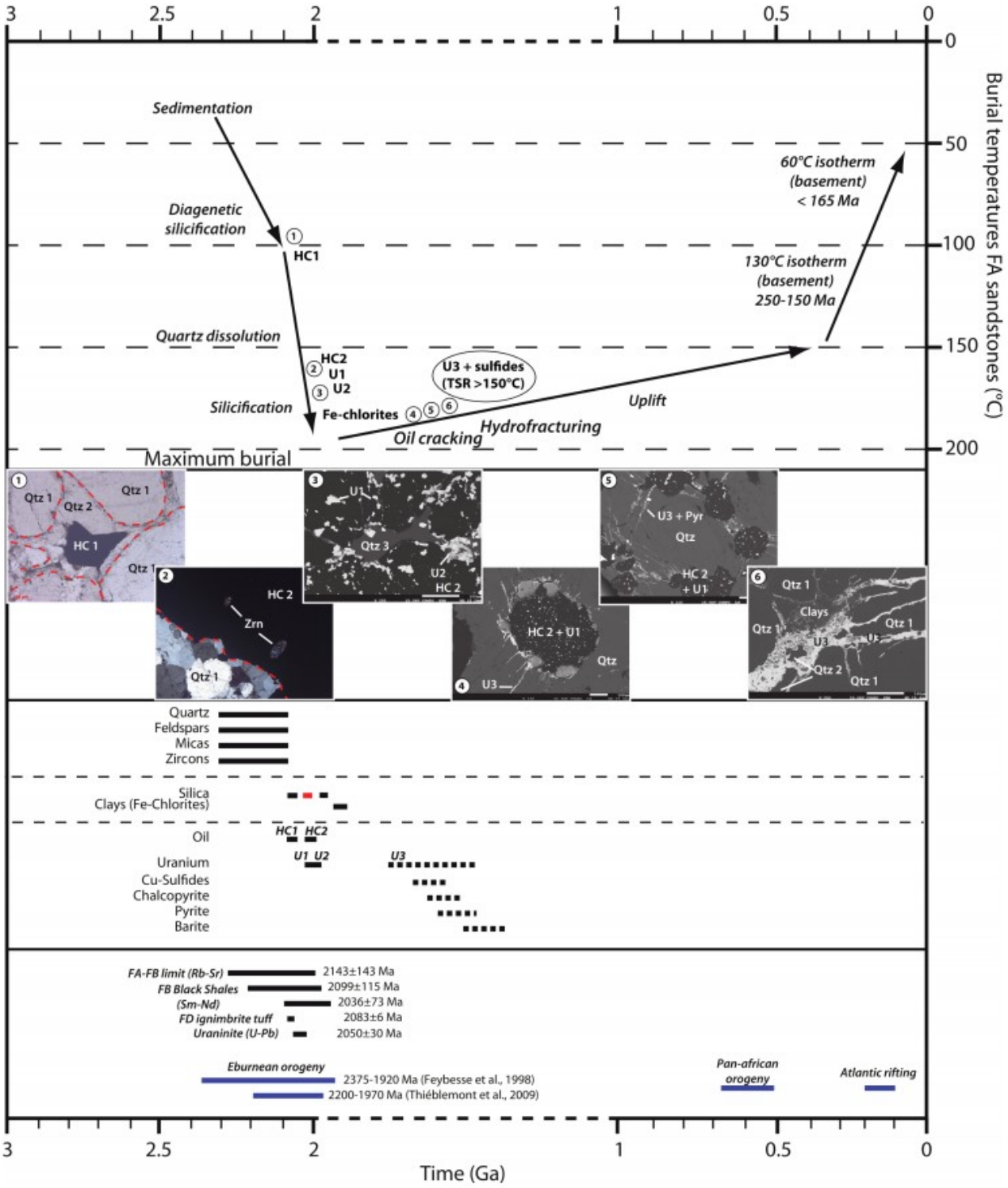

Fig. 15. Summary diagram of oil migration and uranium mineralization in FA sandstones. Additional age data are summarized in Gauthier-Lafaye (2006). Orogeny ages are from Feybesse *et al.*, 1998 and Thiéblemont *et al.*, 2009.A complete list of previous data can be found in Mathieu (1999).